



Review

Photocatalytic H₂O₂ production Systems: Design strategies and environmental applicationsZhong Chen ^{a,b}, Ducheng Yao ^{a,b}, Chengcheng Chu ^{a,b}, Shun Mao ^{a,b,*}^a College of Environmental Science and Engineering, Biomedical Multidisciplinary Innovation Research Institute, Shanghai East Hospital, State Key Laboratory of Pollution Control and Resource Reuse, Tongji University, 1239 Siping Road, Shanghai 200092, China^b Shanghai Institute of Pollution Control and Ecological Security, Shanghai 200092, China

ARTICLE INFO

ABSTRACT

Keywords:

Hydrogen peroxide
Photocatalytic synthesis
Design strategy
Fenton reaction
Disinfection
Pollutant degradation

Hydrogen peroxide (H₂O₂) is an environmentally friendly versatile oxidant, which has been used in chemical industry, medical, energy, and environmental fields. Photocatalytic H₂O₂ production is a sustainable, safe, and green process; however, the high recombination of electron-hole pairs, low visible light utilization, and poor product selectivity still limit the practical applications of photocatalytic H₂O₂ production. Previous reviews on photocatalytic H₂O₂ generation focus more on the photocatalysts but less on the design strategy of the photocatalytic systems, which stems from the critical steps involving the photocatalytic process, i.e., light absorption, charge separation, and surface redox reaction. From this point of review, this review article introduces the strategies for improving the H₂O₂ production efficiency based on the above three critical processes. Moreover, the environmental applications of photocatalytic H₂O₂ generation including disinfection and pollutant degradation are discussed. The challenges and prospects in photocatalytic H₂O₂ production and its future environmental applications are also envisioned.

1. Introduction

Hydrogen peroxide (H₂O₂), as one of the 100 most important chemicals in the world, has attracted increasing attention since its first synthesis by Thenard in 1818 [1]. It has been widely used in chemical industry [2,3], medical [4,5], energy [6,7], and environmental fields [8,9]. H₂O₂ is a highly efficient and green oxidant for environmental remediation applications due to its high content of active oxygen and safe reaction product (H₂O and O₂). It is usually used as a supplement of oxygen source in the bioremediation of polluted aquifers [10] and as an oxidizing agent in advanced oxidation processes (AOPs) [11], which can produce •OH through Fenton reaction or under UV radiation [12,13]. H₂O₂ is also used in water disinfection without producing disinfection byproducts, which will be generated by using traditional chemical disinfectants such as chlorine, ozone, chloramines, and chlorine dioxide [14,15].

At present, oxidation of anthraquinone (AQ) is the mainstream technology for the industrial production of H₂O₂. However, the AQ oxidation process requires high energy input and produces a large amount of wastewater due to the multistep hydrogenation and oxidation

reactions [1,16]. Direct synthesis of H₂O₂ from H₂ and O₂ can be realized through catalytic synthesis with noble metal catalysts [17–19]. Unfortunately, the high cost, low H₂O₂ selectivity, and the explosion risk of H₂/O₂ mixture in this reaction make it hard to scale up this technology to industrial applications [20,21]. Thus, an environmentally friendly and safe process for the production of H₂O₂ is highly desired. Photocatalytic H₂O₂ production driven by solar energy is one of the most promising methods, which only needs earth-abundant water and oxygen as raw materials and renewable sunlight as energy supply. Particularly, it can produce H₂O₂ on site and on demand, avoiding the risk in the production and transport of dangerous concentrated H₂O₂.

H₂O₂, as the unique stable molecule ROS, has a much longer lifetime than other ROS in water [22]. Thus, compared with other ROS-based photocatalytic processes, photocatalytic H₂O₂ production system can promote the inactivation efficiency of bacterial by diffusing and penetrating the bacterial membrane through the hydrophilic porin [23]. Moreover, its oxidation capacity can be further boosted by Fenton or Fenton-like reaction for refractory pollutant degradation. The H₂O₂ utilization and pollutant degradation efficiency of the photocatalytic H₂O₂ generation-based Fenton system was reported to be higher than

* Corresponding author at: College of Environmental Science and Engineering, Biomedical Multidisciplinary Innovation Research Institute, Shanghai East Hospital, State Key Laboratory of Pollution Control and Resource Reuse, Tongji University, 1239 Siping Road, Shanghai 200092, China.

E-mail address: shunmao@tongji.edu.cn (S. Mao).

those of the traditional Fenton systems [24,25].

However, the high recombination of electron-hole pairs, low visible light utilization and product selectivity still limit the practical applications of photocatalytic H₂O₂ production. Currently, commonly used photocatalysts such as TiO₂ and g-C₃N₄ inevitably have these problems [26,27]. In the past few years, various strategies were proposed to improve the photocatalytic activity of catalysts for H₂O₂ production and many exciting results have been achieved that merit a timely review on the recent advances in photocatalytic H₂O₂ production and its environmental applications. Previous review articles have summarized the development of photocatalysts in photocatalytic H₂O₂ production including carbon nitride [28–30], Au nanoparticle (NP)-based plasmonic photocatalysts [31], carbon materials [32], inorganic metal-oxides [33]. Other reviews also summarized the various catalysts with different modification methods [16] or reaction pathways [34] and compared their application for photocatalysis and electrochemistry [35]. However, those reviews focus more on the photocatalyst but less on their design strategy based on the fundamental mechanism and their application.

The photocatalytic H₂O₂ synthesis process involves multiple steps including light absorption, charge carrier excitation/trapping/separation/transfer, reactant surface adsorption, surface redox reaction, intermediate conversion, and product stabilization/desorption [36–38]. These critical steps intrinsically determine the overall efficiency of H₂O₂ generation. Herein, we summarize the design strategies for efficient photocatalytic H₂O₂ production based on the three main processes including light absorption, charge separation, and surface redox reaction. Additionally, the applications of photocatalytic H₂O₂ production in

environmental fields including disinfection and pollutant degradation have been discussed and highlighted. Finally, prospects of H₂O₂ production in the sustainable environment and outlooks on future research directions are given. This review aims to inspire new ideas in the design of high-performance photocatalytic systems for H₂O₂ production and broaden its applications in the environmental field.

2. Fundamental processes of photocatalytic H₂O₂ production

As shown in Fig. 1, the typical photocatalytic H₂O₂ production process involves three main steps including light absorption, charge separation, and surface redox reaction. Firstly, the photocatalysts absorb photons under light illumination, and electrons are excited from the VB to the CB when the energy is greater than the bandgap (E_g). In the second step, the electron and hole pairs will separate and migrate, but most of them will recombine and only a few can transfer to the surface of the photocatalyst. Finally, the separated electrons and holes participate in the surface redox reactions mainly including oxygen reduction reaction (ORR) and water oxidation reaction (WOR) to produce H₂O₂.

The reaction potentials of the corresponding ORR and WOR are shown in Fig. 1. The ORR can be classified as 2e⁻ ORR (including indirect (I and IV) and indirect (II) pathway) and 4e⁻ ORR pathway (III) according to the electron transfer number and reaction intermediates. The CB of photocatalyst for H₂O₂ production through the 2e⁻ ORR pathway must be more negative than 0.68 V. It is thermodynamic forbidden for indirect 2e⁻ ORR when the CB is between + 0.68 V and -0.33 V. The direct and indirect 2e⁻ ORR usually coexist when the CB is more negative than -0.33 V. The direct 2e⁻ ORR with more positive

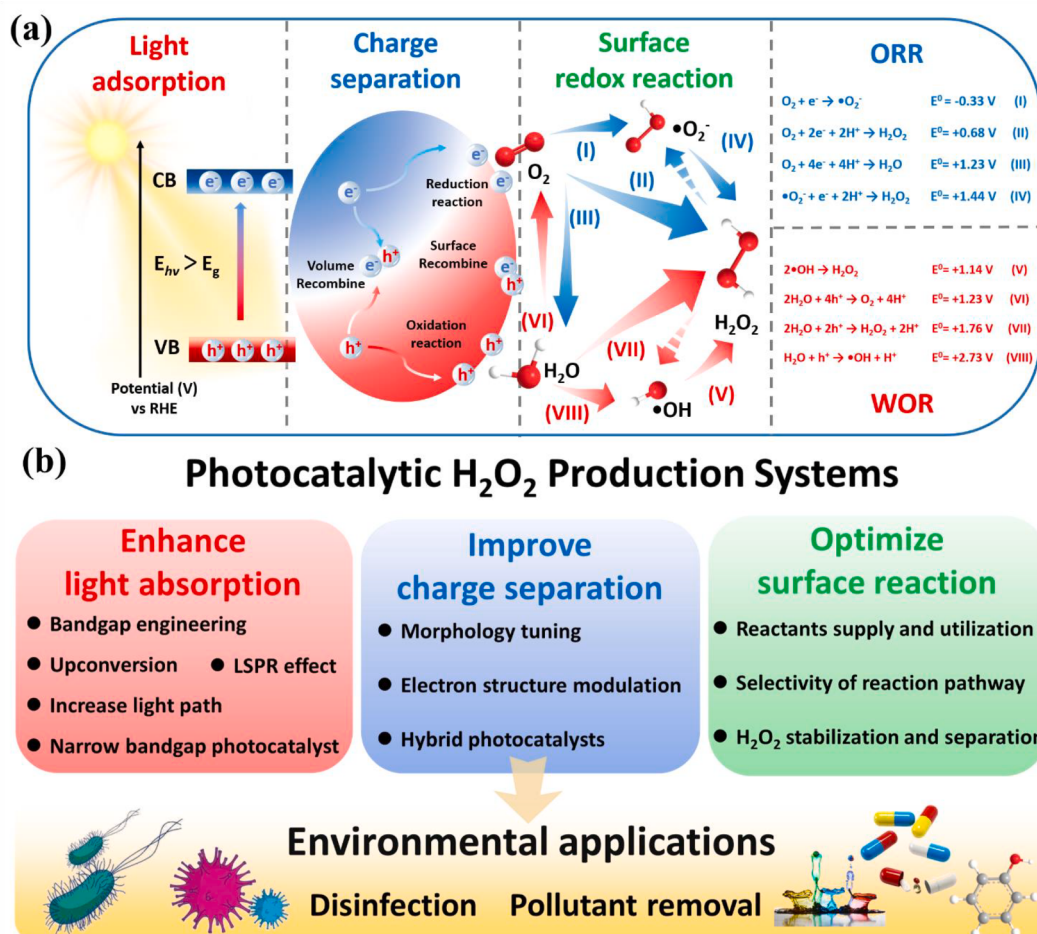


Fig. 1. (a) Schematic illustration of the three fundamental processes in photocatalytic H₂O₂ production. (b) The topic map of this review.

reaction potential is favorable in thermodynamics, while the indirect $2e^-$ ORR that requires only one electron in each step is favorable in kinetics. Notably, the $4e^-$ ORR with more positive reaction potential may take place during all ORR processes; thus, it is vital to increase the selectivity of $2e^-$ ORR for H_2O_2 production. Similarly, the WOR can also be classified as $2e^-$ WOR (including direct (IV) and indirect (V) pathway) and $4e^-$ WOR pathway (VI). Theoretically, the VB of photocatalyst for H_2O_2 production through WOR must more positive than 1.76 V. The direct WOR pathway is more favorable in thermodynamics and the indirect WOR pathway is more favorable in kinetics.

The dual-channel H_2O_2 evolution that integrates both ORR and WOR pathways is preferred as it produces H_2O_2 from O_2 and H_2O without sacrificial agents. In this process, the H^+ or O_2 produced through WOR can participate in the ORR and the consumption of electrons in ORR will leave more h^+ for WOR. Theoretically, the atom utilization efficiency can reach 100 % by integrating $2e^-$ ORR and $2e^-$ WOR. However, the synthesis of H_2O_2 on the photocatalyst surface is usually accompanied by the decomposition of H_2O_2 . In the further reduction or oxidization of H_2O_2 , the O—O bond will dissociate to form $\bullet OH$ or $\bullet O_2^-$ [22]. Besides, the produced H_2O_2 will decompose under the illumination of ultraviolet light [39]. Therefore, some special strategies have been utilized to stabilize H_2O_2 and separate it from the photocatalyst once produced.

To sum up, the light absorption, charge separation, and surface redox reaction of the photocatalyst are the vital processes determining the efficiency of H_2O_2 production. Therefore, all these processes should be considered comprehensively to design an efficient photocatalyst for H_2O_2 production. In the next section, we will review the design strategies of photocatalysts for efficient H_2O_2 production from these three main processes.

3. Design strategies for the catalytic system

3.1. Enhancing light absorption

The light absorption capacity of a photocatalyst is one of the prime factors affecting the efficiency of photocatalytic H_2O_2 production. It controls the total number of charge carriers that will be photogenerated and the maximum utilization efficiency of nature sunlight. The photocatalytic activity of a photocatalyst is closely related to the intensity and spectrum of the light source, and generally, the performance is boosted under stronger light intensity because of the resulting large number of photons. However, a semiconductor photocatalyst can only absorb light with energy equal to or greater than its band gap. Therefore, expanding the light absorption range and enhancing the light utilization capacity of

Table 1
Strategies to enhance the light absorption of photocatalysts for H_2O_2 production.

Strategy	Photocatalyst	Light source	Reaction solution	Absorption edge (nm)	Bandgap (eV)	H_2O_2 ($\mu\text{mol h}^{-1} \text{g}^{-1}$)	AQY (%)	SCC (%)	Ref.
Bandgap engineering (heteroatoms doping and defect introduction)	Carbon vacancy contained g-C ₃ N ₄	$\lambda > 420$ nm	Water	460 (enhancement in 300–800 nm)	2.68	~90	–	–	[44]
	Reduced g-C ₃ N ₄	$\lambda > 420$ nm	Water	460	2.69	170	4.3 (420 nm)	0.26	[45]
	PCNBAs ^a	$\lambda > 420$ nm	Water	510	2.43	~90	8.0 (420 nm)	0.3	[40]
	AKMT ^b	$\lambda > 420$ nm	10 % ethanol	490	2.52	~3600	100 (320–450 nm)	–	[42]
	PCN-NaCA ^c	Simulated sunlight	3.5 wt% glycerol aqueous solution	460	2.69	18,700	11.8 (420 nm)	–	[36]
Conversion of low energy photons (upconversion)	GOND/CdS/TTA-UC ^d	$\lambda = 635$ nm	5 % alcohol	~500	–	192	–	–	[48]
	α -Fe ₂ O ₃ /CQD@g-C ₃ N ₄ ^e	$\lambda > 420$ nm	Water	~800	–	138.6	17.8 (420 nm)	–	[49]
	CoP/CDS ^f	420–700 nm	Water	>700 nm (enhancement in 200–800 nm)	1.73	466	–	–	[50]
	SnS ₂ /In ₂ S ₃ /CDS	$\lambda > 420$ nm	Water	~650 (enhancement in 500–800 nm)	–	1111.89	0.6 (420 nm) 3.9 (535 nm)	1.02	[51]
LSPR effect	Bimodal-Au/TiO ₂ -CO ₃ ²⁻	$\lambda > 430$ nm	4 % HCOOH	apparent LSPR peak at 566 nm	–	~1000	5.4 (530 nm)	–	[53]
	Ag@U-g-C ₃ N ₄ -NS	Visible light	Water	>1200	–	118.5	–	–	[54]
	CN-Au/BiVO ₄	$\lambda > 420$ nm	Citrate buffer solution	~550 (new shoulder peak at 620 nm)	–	675.89	–	–	[55]
Increase light path and residence time	NCNT ^g	$\lambda > 420$ nm	10 % ethanol	~470 (enhancement in 450–800 nm)	2.62	485.7	–	–	[56]
Narrow bandgap photocatalyst	In ₂ S ₃ @Ov/In ₂ O ₃	Visible light	Water	~570	–	275.4	28.9 (420 nm)	–	[57]
	PC-MB ^h	$\lambda > 420$ nm	Water	660	1.88	1385.42	1.44 (630 nm)	–	[58]
	RF523 resins	AM 1.5 G	Water	620	2.0	2.475	~8 (420 nm)	0.5	[59]
	Defective ZrS ₃ nanobelts	AM 1.5 G	33.3 mM benzyl alcohol	626	1.98	1792	11.4 (400 nm) 10.8 (500 nm)	–	[61]
	PM-CDs ⁱ	$\lambda > 420$ nm	Seawater	640	1.94	1776	0.54 (630 nm)	0.21	[62]

^a PCNBAs: polymeric carbon nitride copolymerized by melem and barbituric acid.

^b AKMT: S and K doped melon-based C₃N₄ photocatalysts with periodic heptazine conjugation.

^c PCN-NaCA: polymeric carbon nitride framework with sodium cyanamate moiety.

^d GOND: graphene oxide nanodisk; TTA-UC: sensitized triplet-triplet annihilation upconversion chromophore-containing silica nanocapsule.

^e CQD: carbon quantum dot.

^f CDs: carbon dots.

^g NCNT: 3D hierarchical network of carbon nitride tubes.

^h PC-MB: procyanidin-methoxy-benzaldehyde.

ⁱ PM: photocatalyst composed of procyanidins and 4-methoxybenzaldehyd.

the photocatalyst is a direct mechanism to improve the efficiency of photocatalytic H_2O_2 production under solar light illumination. In this section, the different strategies adopted to enhance the absorption capacity of photocatalysts for H_2O_2 production are overviewed (Table 1).

One of the commonly used strategies involves doping with hetero-elements and introducing defects. Several reports in the literature confirmed that doping with foreign elements enhances the light absorption capability of photocatalysts [40–42]. This is generally realized through a smaller intrinsic bandgap by perturbing the hybrid orbital and rearranging the band structure of the photocatalysts. The dopant can be incorporated into the crystal lattice of the catalyst, forming impurity energy levels, which results in a narrowed band gap [43]. For example, the absorption edge of O element doped polymeric carbon nitride (PCN) has been expanded from approximately 450 nm to 570 nm with the reduction of its bandgap from 2.77 to 2.18 eV, as shown in Fig. 2a [40]. In another report, g-C₃N₄ modified with KOH and KCl (AKCN) exhibited nearly 100 % apparent quantum yield (AQY) in the range of 320–420 nm with alcohol or glucose as electron and proton donors [41]. The H_2O_2 production at 1.37 mM/h with 100 % AQY at the wavelength range of 360–450 nm has been achieved and that nearly 40 % AQY at 500 nm was maintained upon doping g-C₃N₄ catalyst with K and S atoms [42]. Notably, heteroatom dopants usually cause the breakage and

formation of chemical bonds, thereby unavoidably introducing vacancies.

The mechanism of improving photocatalytic light absorption via introducing defects is different from heteroatom doping. The vacancy will reduce the symmetry of catalyst, leading to the electron delocalization effect and producing more electrons [44]. Those photons with lower energies than the bandgap can be absorbed by the introduced intermediate energy levels (Fig. 2b), which promote light harvesting and extend the absorption range [45–47]. Therefore, the presence of defects has limited influence on the intrinsic bandgap energy of the photocatalyst, which is usually manifested by stronger absorption tails in the visible region rather than extended absorption edge. Notably, the improved photocatalytic efficiency of H_2O_2 production through the introduction of heteroatoms and vacancies may also be attributed to the separation of photogenerated charge carriers and the selectivity of surface redox reactions, which will be discussed in the next sections.

Converting low-energy photons to high-energy photons via the upconversion process is another effective strategy to utilize the wasted photons for H_2O_2 production. To give particular examples, Kim *et al.* [48] reported a ternary nanohybrid catalyst that achieved H_2O_2 production of 100 $\mu\text{M}/\text{h}$ under red laser irradiation of wavelength $\lambda = 635 \text{ nm}$ via sensitized triplet-triplet annihilation (TTA)

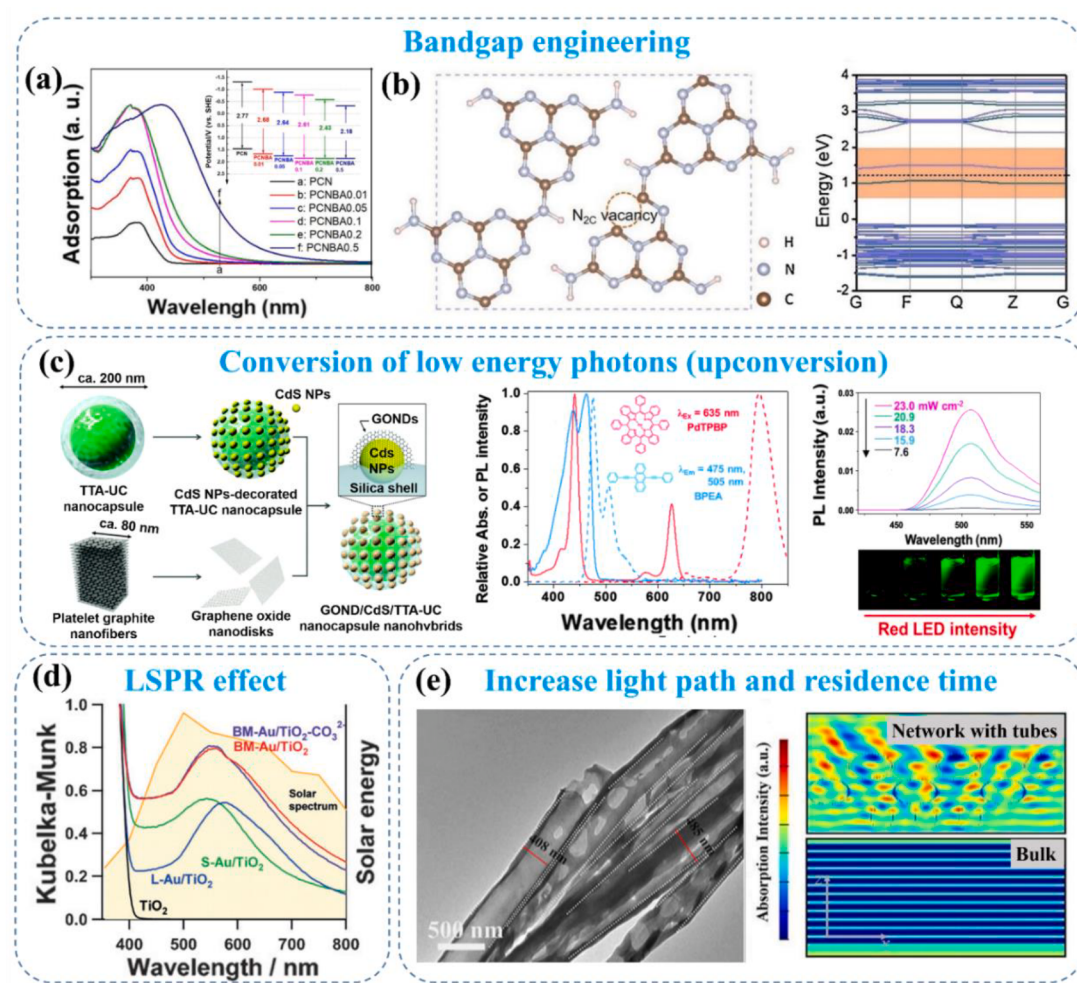


Fig. 2. (a) UV-vis spectra and band positions of polymeric carbon (PCN) and polymeric carbon nitride copolymerized by 2,5,8-triamino-tri-s-triazine (melem) and barbituric acid (PCNBA). Reprinted with permission from [40]. Copyright 2020, Elsevier. (b) Structure models and calculated band structures of PCN with $\text{N}_{2\text{C}}$ vacancy. Reprinted with permission from [47]. Copyright 2020, Elsevier. (c) Schematic illustration graphene oxide nanodisk/CdS/triplet-triplet annihilation upconversion chromophore-containing silica nanocapsule (GOND/CdS/TTA-UC) and its upconversion mechanism. Reprinted with permission from [48]. Copyright 2016, Royal Society of Chemistry. (d) UV-vis spectra of the photocatalysts. Reprinted with permission from [53]. Copyright 2016, John Wiley and Sons. (e) TEM image and electrical field intensity distribution of 3D network of carbon nitride tubes (NCNT). Reprinted with permission from [56]. Copyright 2021, John Wiley and Sons.

upconversion technique. The authors employed two kinds of chromophores as sensitizer and acceptor to bring about the upconversion of red light to green light. As depicted in Fig. 2c, the Q-band (575 and 635 nm) of tetraphenyltetrazeno-porphyrin (PdTPBP) can be selectively excited under red light and the sufficiently separated absorption edge of 9,10-bis (phenylethynyl)anthracene (BPEA) achieves the red-to-green ($\lambda_{\text{max}} = 505$ nm) upconversion. Similarly, CDs with fluorescence can convert the visible light and even near-infrared light of about 800 nm wavelength to the absorption edge of carbon nitride at around 450 nm [49]. So, photocatalysts coupled with CDs usually exhibit significantly enhanced light absorption in the visible and even near-infrared regions [50,51]. Besides, injecting hot electrons by means of localized surface-plasmon resonance (LSPR) effect is also a practical approach to utilize the wasted low-energy photons. Metal nanoparticles such as Au, Ag, and Cu can produce energetic hot electrons with higher energy than the interface Schottky barrier through the LSPR effect under light illumination, which can be directly injected into the host semiconductor [52], thereby improving the absorption of the photocatalyst to visible light or even near-infrared region (Fig. 2d). Therefore, doping with metal nanoparticles can have a pronounced effect on the light absorption performance of various photocatalysts including TiO₂ [53], g-C₃N₄ [54], and other metal oxides [55].

In addition to aforementioned approaches, making full use of the available limited number of photons is another useful mechanism that may be adopted. Here, the limited number of light photons can be fully utilized by increasing the light path and residence time of photons in the photocatalyst; for instance, via facilitating the absorption of initially unabsorbed photons through multiple scattering in the pores and channels of a photocatalyst until saturation. A case in point is the 2.1-fold light absorption proficiency in the wavelength range of 450–800 nm achieved by the photocatalyst C₃N₄ tubes with three-dimensional hierarchical networks (NCNT, Fig. 2e), was attributed to the accelerating light reflection inside the tube channels to increase the light path distance and residence time [56]. Simulation results corroborated the claim of the inner multistage light scattering and reflection at the tube-air and tube-tube interface of the NCNT. Similarly, the enhanced light absorption efficiency demonstrated by In₂S₃@In₂O₃ catalyst, with AQY of H₂O₂ production in pure water reaching 28.9 % at 420 nm, was ascribed to the porous tubular structure of the catalyst [57].

The most direct route to improve the light absorption capacity of a photocatalyst is to develop narrow-band gap photocatalysts. Metal-free organic photocatalysts have recently drawn increasing attention from researchers owing to the cost and potential environmental damage associated with metal catalysts. For example, the metal-free organic catalyst, procyanidin-methoxy-benzaldehyde (PC-MB), with a narrow bandgap value of 1.88 eV exhibited good absorption performance in a wide light region, giving H₂O₂ production rate of 1385.42 μmol h⁻¹ g⁻¹ [58]. In another research report, resorcinol-formaldehyde (RF) resins with a band gap of 2.00 eV absorbed broad-wavelength of light and produced H₂O₂ with >0.5 % solar to chemical conversion efficiency (SCC) [59]. Recently, Liu *et al* [60] investigated the photocatalytic performance of 60 candidate materials including covalent organic frameworks (COFs), small molecules, linear conjugated polymers (LCPs), and conjugated microporous polymers (CMPs). They observed that most candidates produced H₂O₂ from pure water under simulated sunlight, but the compounds get decomposed during the cycling experiment. This indicates the importance of considering the long-term stability of organic photocatalysts when applied for H₂O₂ production.

Although several strategies have been adopted and reported to enhance the light absorption capacity of various photocatalysts, further work is still required to address the drawbacks in each strategy and efficiently boost their performance. Heteroatom doping and defects in photocatalysts can enhance their light absorption capability by adjusting the band gap structure. However, their effect on the longer wavelength region is still limited. That is the reason why some modified

photocatalysts can reach 100 % AQY in the ultraviolet region but this decreases rapidly and almost approaches zero when the wavelength is above 500 nm. Meanwhile, the modification strategies utilizing low energy photons through upconversion or LSPR effect are restricted by the complex preparation process. As for the narrow-band gap photocatalysts, most of which are organic catalysts, stability is an issue that need to be considered for their long-term utilization.

3.2. Improving charge separation

The efficient separation, transport, and interfacial transfer of photo-induced charge carriers in photocatalysts is another critical factor that determines their overall performance of H₂O₂ production. The separation of the carriers under light irradiation is usually random, and due to the hindrance from carrier recombination, only a few charges can reach active sites to participate in the reaction to give H₂O₂. To suppress the charge carriers' recombination problem, sacrificial agents are often utilized, but this could make the process infeasible and uneconomical in practical environmental applications. As such, the issue of efficient charge carrier separation has been a research hotspot in recent years.

Controlling the directional transfer of electrons has been proposed to be a promising approach to restrain the recombination of photo-generated electron-hole pairs. Some specific morphologies of the catalysts are favorable for directional electron transport. For example, high-curvature structures can concentrate local electric fields on the tip area, inducing the electron transfer along the raised tips [63,64]. The nonsymmetrical internal electric field in a photocatalyst can also induce the directional movement of charges, accelerating their separation and transfer. Zeng *et al.* [64] used such “lightning rod effects” to construct a 3D branched C₃N₄ with nanoneedle structures so as to manipulate the separation and transfer of electron-hole pairs and improve the rate of H₂O₂ production. The two-dimensional (2D) structure is beneficial for charge transfer to the surface of photocatalysts, and exfoliating bulk g-C₃N₄ into 2D nanosheets is an effective strategy to accelerate the rate of charge transfer. The resulting reduced stacking layer and larger specific surface area can shorten the electron diffusion paths, accelerate migration to the surface, and enhance the surface carrier density [16,65,66]. However, the unavoidable concurrent quantum size effect could influence the bandgap structure of g-C₃N₄ and result in reduced light absorption, and some strategies such as doping with S or P elements, to optimize the band structure and compensate for the light absorption loss and also accelerate the charge transfer rate in g-C₃N₄ nanosheets, have been adopted for photocatalytic H₂O₂ production [65,66].

Defect engineering is another commonly used strategy for improving the charge separation. A series of defect engineering such as C [44], N [46,47,67], S vacancies [61], and cyano (C≡N) group defects [45,67] have been reported to achieve marked charge carriers separation efficiency. The introduced defects and the localized states in bandgaps can act as electron capture centers to trap the CB electrons and accelerate the migration of charges through the internal electric field, thereby participating in the further reactions of H₂O₂ production (Fig. 3a) [46]. The unsaturated atoms due to the presence of vacancies can also act as paramagnetic centers to attract photoelectrons and avoid their recombination with holes [44]. Moreover, functional groups with high electrophilicity (such as C≡N) can induce more localized distribution of charges, achieving efficient carrier separation [45]. Nonetheless, the defect states can also act as the electron recombination centers and induce the lowering of the CB position, which may decrease the number and reductive ability of the photogenerated electrons. Therefore, the accurate control of the number and position of vacancies is crucial for promoting the efficiency of charge separation.

Heteroatoms can act as electron receptors to increase the local electronic density and decrease the work function of the photocatalyst by facilitating the escape of electrons from its surface. Further, elemental doping and defects can synergistically adjust the electron structure and improve the charge separation efficiency. Interlaminar

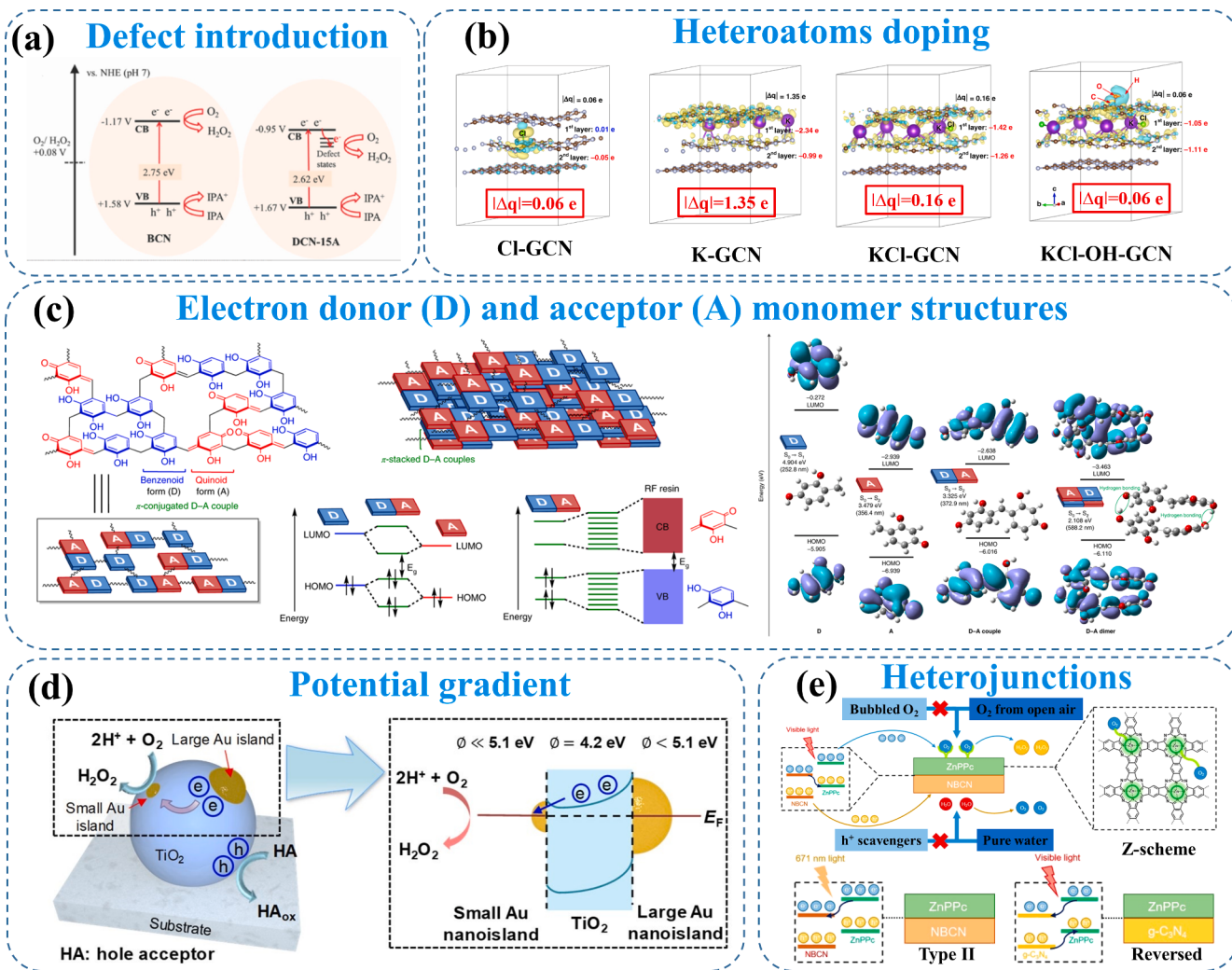


Fig. 3. (a) Schematic of photocatalytic H_2O_2 evolution mechanism over bulk $\text{g-C}_3\text{N}_4$ (BCN) and nitrogen defective $\text{g-C}_3\text{N}_4$ (DCN). Reprinted with permission from [46]. Copyright 2018, John Wiley and Sons. (b) Charge distribution analysis of photocatalysts. Reprinted with permission from [41]. Copyright 2019, Springer Nature. (c) Structure and energy diagrams and interfacial plots of resorcinol-formaldehyde resins. Reprinted with permission from [59]. Copyright 2019, Springer Nature. (d) Proposed mechanism of potential gradients for H_2O_2 production on Au/TiO_2 . Reprinted with permission from [75]. Copyright 2019, American Chemical Society. (e) Electron transfer pathway in different types of heterojunctions. Reprinted with permission from [77]. Copyright 2021, National Academy of Science.

space is one of the main barriers to efficient charge separation, and the positive impacts of defects and heteroatoms on the interlayer charge transfer have been investigated. As shown in Fig. 3b, the interlayer bridging effect of K atoms cause electron density polarization on the first layer, and the Cl atoms and OH group can balance the electron distribution and decrease the charge difference between the adjacent layers ($|\Delta q|$) to facilitate the interlayer charge migration [41]. This inhomogeneous distribution of electrons is in favor of the sequential reactions of electrons and holes at different sites. Additionally, the synergistic effects of S substitution and K bridging can further promote the polarization of trapped electrons and interlayer charge separation [42].

Constructing electron donor (D) and acceptor (A) monomer structures in polymer photocatalysts is another used methodology to prompt the directional migration of electrons and holes and enhance their extent of separation. For instance, the π -conjugation and π -stacked D-A structure in resorcinol-formaldehyde (RF) resins have extended the π -delocalization and hybridized the energy levels of benzenoid and quinoid units, forming a low bandgap (Fig. 3c) [59]. The HOMO and LUMO electrons are mainly located in the D and A units, respectively, which are conducive to efficient charge separation. The SCC efficiency of RF can reach 0.5 %, which is higher than that of the natural photosynthesis of plants (~0.1 %) [68].

Another possible strategy that may be employed for inducing effective charge separation in a photocatalyst is by coupling it with various components. Quantum dots (QDs) can raise the rate of H_2O_2 formation due to their unique properties of electron transfer and storage [51,69–72]. They can promote the carrier separation efficiency by regulating the charges on the multi-interface and decreasing the resistance of electrons transfer between components [51]. The storage and secondary discharge of electrons by CDs can further stabilize the excited electrons and slow down their recombination [72,51]. The presence of metal cations ionizes the surface functional groups of CDs, and this hinders the electron-hole recombination in PC-MB catalyst by increasing its charge and electron sink barrier [62]. The composite photocatalyst demonstrated high photocatalytic activity ($1776 \mu\text{mol h}^{-1} \text{ g}^{-1}$) for H_2O_2 production in real seawater. In our previous study [73], we obtained H_2O_2 production rate of $703.4 \mu\text{M g}^{-1} \text{ h}^{-1}$ using $\text{SnO}_2/\text{g-C}_3\text{N}_4$ composite as a photocatalyst, which is about 5 folds in magnitude compared to that achieved by pure $\text{g-C}_3\text{N}_4$. This pronounced performance of the composite catalyst as compared to the pure $\text{g-C}_3\text{N}_4$ catalyst is due to the more efficient electron-hole pairs separation in the composite, with $\text{g-C}_3\text{N}_4$ acting as CB electron donor and SnO_2 electron acceptor components. In addition, it has been found that coupling with noble metal NPs improved the π -conjugated structure in $\text{g-C}_3\text{N}_4$ by engendering uniform

distribution of electrons so as to optimize the electron structure for successful charge separation and transfer [74]. Noble metal NPs can also effectively inhibit the recombination of photogenerated carries by scavenging electrons to form a Schottky barrier [54]. Further, the size of noble metal NPs can impact their work functions and Schottky barriers and that the formed potential gradients between different sized NPs drives the electron transfer to the smaller sized NPs with lower potential barriers, thereby promoting the rate of H₂O₂ production efficiency, as illustrated in Fig. 3d [75].

Besides the above proposed strategies, the construction of heterojunctions has been proved to be one of the most efficient ways for the spatial separation of electron-hole pairs. In this method, electrons excited in one catalyst are transferred to the other catalyst, giving rise to long-lived electron-hole pairs. Liu *et al.* [76] studied the effect of heterojunction coverage on charge separation competence and photocatalytic H₂O₂ production yield. The spatially separated structure and type II electron transfer pathway promotes better charge separation efficiency. For example, the NH₂-MIL-125@ZnS with suitable heterojunction coverage shows the highest H₂O₂ production rate of around 120 mM g⁻¹ h⁻¹. Ye *et al.* [77] constructed the Z-scheme heterojunction of zinc polyphthalocyanine (ZnPc) and modified carbon nitride (NBCN) with close Fermi levels for the first time (Fig. 3e). Their study presented a strategy for constructing Z-scheme heterojunctions between two semiconductors with close Fermi levels. They verified that the electron transfer pathway of type II and Z-scheme can be tuned by excitation wavelengths. Thus, the ZnPc-NBCN exhibited higher O₂ evolution activity from water oxidation, avoiding the use of sacrificial electron donors. However, not all heterojunction band alignments are appropriate for ORR and WOR potential of H₂O₂ production. The more ideal structure for H₂O₂ production may be Z-scheme, which can provide more negative and positive potential positions for ORR and WOR, respectively to improve the H₂O₂ production efficiency. Moreover, the reaction pathway for H₂O₂ formation may be affected by matching the energy band gaps of the components forming the heterojunction, as it will be discussed in the next section.

In summary, charge carrier separation can be promoted by directional electron transfer mainly through internal polarization of electric field or coupling with other components. Heteroatom doping and defect control are the main strategies to cause electron polarization. It is necessary to select suitable elements for substitution/doping purpose for the accurate control of defects in order to avoid their potential detrimental role as photoelectron recombination centers. The complex interactions between different components determine the direction of carrier migration, which will further affect the subsequent redox reactions. Therefore, it is immensely important to further explore the charge transfer mechanism to be able to guide the design and selection of appropriate components of a photocatalyst.

3.3. Optimizing surface reaction

Although multiple complex redox reactions happen in photocatalytic systems, the consistent design strategy is to promote the production of H₂O₂ and avoid its decomposition. This is primarily achieved through increasing the supply and utilization of reactants, optimizing the reaction pathway, and improving the stability and desorption of final products, each of which are discussed as under.

3.3.1. Supply and utilization of reactants

As depicted in Fig. 1, oxygen reduction to synthesize H₂O₂ is a proton coupled electron transfer process, and the supply of oxygen, protons, and electrons is essential for the efficiency of ORR. Generally, oxygen aeration, acidic conditions, the addition of protons, and electron donors (such as alcohols) in the photocatalytic system can provide adequate O₂, H⁺, and e⁻ to induce the ORR. However, it is uneconomical and have, to some extent, limited practical application. Thus, it is a promising method to improve the utilization rate of limited reactants for H₂O₂

production in the natural condition by some modification strategies on materials.

Improving the utilization of O₂ and H⁺ is usually achieved through maximizing their adsorption on the surface of the catalyst material. The structure of the employed photocatalyst with smaller particle size and larger specific surface area can provide more abundant active sites for adsorption and activation of oxygen. For example, the polymerization terminated PCN (TP-PCN) with abundant edge active sites (AEASs) showed noticeably lower adsorption energy of oxygen and achieved a superior H₂O₂ production rate of 3265.4 μM h⁻¹ [78]. The availability of AEASs in TP-PCN allowed more transition states and β spin-orbital with a higher orbital contribution to excited states, and this, in turn, optimizes the transfer of electrons to the π* orbital of O₂ facilitating its activation (Fig. 4a). Dopant elements and defects can also boost the oxygen adsorption capacity and oxygen activation for H₂O₂ production. As mentioned earlier, heteroatom dopants can cause electron polarization and create new active sites to which O₂ is preferably attracted, and this is more obvious in the substitution between atoms with greater difference in electronegativity, exhibiting more negative adsorption energy for O₂ (Fig. 4b). These polarized electrons would transfer from the conjugated rings to the antibonding π* orbital of adsorbed *O₂ under the strong electron pushing effect, which further weakens the O—O bond and facilitates its protonation in subsequent ORR [42]. Similarly, the more electronegative N atoms, up on substituting for C atoms in graphene, can bring about the transfer of electrons from adjacent C atoms. Then, the resulting atoms with positive charge density can increase the molecular oxygen adsorption and act as potential ORR active sites [70]. Atoms with a larger atomic radius and lower electronegativity can change the charge and spin densities of the material by substituting for N or C atoms because of their 3p lone pair of electrons [79]. They can also promote the selective adsorption of O₂ by providing unoccupied 3d orbitals to the valence electrons [80]. Similar to heteroatom dopants, the introduced defects can also create highly electron localization nearby the Fermi level, promoting the adsorption of O₂ and H⁺. As reported in our previous study [81], g-C₃N₄, with abundant three coordinate nitrogen (N_{3c}) vacancies (SPCN), was synthesized through a facile sodium persulfate eutectic polymerization method for H₂O₂ production. The strong electronegativity of the N atoms in the C≡N and/or unsaturated C atoms surrounding the N_{3c} defects enhanced the electron-withdrawing ability of SPCN, rendering it possess considerable physical O₂ adsorption capacity (Fig. 4c). The theoretical calculation, outlined in Fig. 4d, further proves that introducing N vacancies can improve the O₂ adsorption capacity of the photocatalyst and promote O₂ activation by decreasing its adsorption energy and changing the bond length, respectively [67]. It also indicates that the adsorption of H⁺ can be enhanced at the N_{2c} and the -C≡N group. Additionally, some substances such as Pd or amine groups [82] with a high nucleophilicity and affinity for oxygen can adsorb O₂ and H⁺, and thus, can be used to modify the surface of a photocatalyst.

To overcome the limitations of the solubility and mass transfer of O₂ in an aqueous media, introducing a gas phase interface in the reaction is potentially beneficial strategy for oxygen in the atmosphere to directly reach the reaction interface. Liu *et al.* [83] developed an air–liquid-solid triphase system for enhanced photocatalytic H₂O₂ production and found about 44 times higher efficiency than that of the traditional solid–liquid diphase system. The enhancement was due to the facilitated reaction at the triphase interface as a result of the hydrophobicity and porous nature of the material. In another study, Li *et al.* [84] utilized COFs with abundant pores to construct a triphase photocatalytic system (Fig. 5a) for the catalytic generation of H₂O₂ in pure water, and obtained a production rate of 2882 μmol h⁻¹ g⁻¹. Here, the authors specified two main factors responsible for the observed higher production rate. Firstly, the large specific surface area of TPB-DMTP-COF (2747 m² g⁻¹) provides abundant reactive sites for oxygen adsorption and reduction. Secondly, water can only wet part of TPB-DMTP-COF but cannot penetrate the carbon fiber paper which leaves the porous structure as gas diffusion

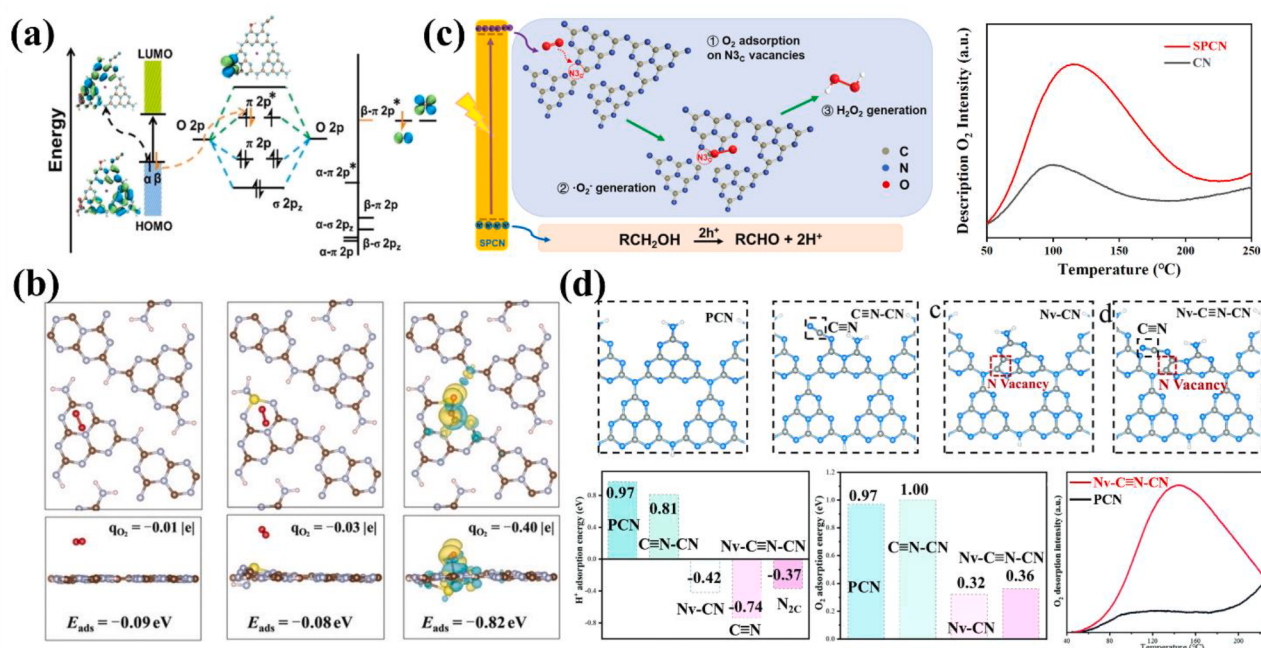


Fig. 4. (a) Mechanism of electron transition from β -HOMO orbitals to O_2 . Reprinted with permission from [78]. Copyright 2021, John Wiley and Sons. (b) Charge densities on the pure melon with different atom substitutions for O_2 adsorption. Reprinted with permission from [42]. Copyright 2020, John Wiley and Sons. (c) Schematic diagram of H_2O_2 generation on $g\text{-}C_3N_4$ with N_{3C} vacancies (SPCN) and temperature programmed O_2 desorption. Reprinted with permission from [81]. Copyright 2022, Elsevier. (d) Effect of $g\text{-}C_3N_4$ models with different defect structures on H^+/O_2 adsorption energy and temperature programmed O_2 desorption. Reprinted with permission from [67]. Copyright 2022, Royal Society of Chemistry.

channels, and thereby significantly enhancing the mass transfer efficiency. Hence, higher concentration of oxygen can closely contact electrons generated by the photocatalyst and the protons from the water at the three-phase interface, enhancing the overall photocatalytic kinetics. Moreover, the Wenzel-Cassie state and tubular confined space formed in the hydrophobic interface greatly boost the interfacial diffusion and transportation of oxygen (Fig. 5b) [85]. In this confined space, sufficient O_2 can participate in the interface reaction to generate H_2O_2 , which could rapidly spread to low-concentration and suppressing its decomposition. As such, the photocatalytic H_2O_2 production in this system is about 10-fold times that of the traditional diphase system through the construction of surface microenvironment engineering. Besides, similar hydrophobic modification and transport channel construction is also feasible in diphase photocatalytic systems [86].

As for H^+ , it can be introduced on the surface of a photocatalyst during its synthesis process or generated through the reaction of surface groups. Ma *et al.* [87] reported a hybrid catalyst titania nanotube with carbon dot (HTNT-CD) for H_2O_2 production from pure water under visible light illumination. Here, it was proposed that the abundant protons formed on HTNT-CD in due process during ion-exchange treatment and the corrosion of citric acid, promoted the positive equilibrium shift of ORR, and the catalyst performed H_2O_2 production rate at $3.42 \text{ mmol g}^{-1} \text{ h}^{-1}$. In a study conducted by Zhou *et al.* [88], they functionalized $g\text{-}C_3N_4$ nanotubes with OH group (ACNT-5) by an alkalization process. As indicated in Fig. 5c, the grafted OH groups serve as electron traps to form surface bound $\bullet\text{OH}$ and produce H^+ .

As for WOR, its reactants are only H_2O and h^+ , and H_2O is usually not a limiting factor when the reactions happen in the aqueous phase. The requirement of the oxidation potential and quantity of h^+ for water oxidation are usually fulfilled through a suitable VB position and efficient charge separation in the photocatalyst. In particular, multiple processes of water oxidation can produce O_2 and H^+ to involve in the ORR and produce H_2O_2 . The electrons consumed by ORR can deter the recombination of charge carriers to some extent and this exposes more h^+ for WOR. Therefore, the dual-channel pathway can theoretically

produce more H_2O_2 by virtue of stimulating WOR and ORR.

3.3.2. Pathway and selectivity of reactions

As discussed in section 2, there are three reaction pathways for H_2O_2 production on the surface of a photocatalyst. In this section, representative photocatalysts of different reaction pathways are overviewed in Table 2.

The main precondition for photocatalytic H_2O_2 production via redox reaction on a photocatalyst surface is to meet the reaction potential of the corresponding ORR and WOR. Thus, the value of the bandgap of the photocatalyst is a good index for determining the redox reaction. For $2e^-$ ORR to produce H_2O_2 , the CB of the photocatalyst must be lower than 0.68 V vs the normal hydrogen electrode (NHE). If the CB lies between -0.33 and 0.68 V, only direct $2e^-$ ORR could proceed. Therefore, discussion about the direct and indirect $2e^-$ ORR is possible only when the CB position is more negative than -0.33 V (vs NHE). To give an example, the CB edge position of TiO_2 is about -0.2 eV [89] and, as such, it is capable of reducing O_2 to H_2O_2 through direct $2e^-$ ORR. As shown in Table 2, those photocatalysts based on TiO_2 usually produce H_2O_2 through the same pathway if the shift of the band gap is not significant. As for $g\text{-}C_3N_4$, its more negative CB allows both direct and indirect $2e^-$ ORR to take place [90], but the formation of 1,4-endoperoxide (Fig. 6a) on $g\text{-}C_3N_4$ facilitates the generation of H_2O_2 through the direct $2e^-$ ORR [91,92]. Thus, photocatalysts based on $g\text{-}C_3N_4$ prefer the same reaction pathway, especially those modification strategies that cause the positive shift in the energy position. Heteroatom doping and defect engineering usually result in the transformation of the reaction pathway from indirect $2e^-$ ORR to direct $2e^-$ ORR due to the positive shift of bandgap and intermediate energy levels. The electron polarization and enhanced O_2 adsorption they induced could facilitate the generation of 1,4-endoperoxide by attracting the triplet O_2 to the para positions. For heterojunctions composed of different semiconductors, the reaction pathway depends on the CB and VB positions that they provide electrons and protons. Luo *et al.* [93,94] utilized nitrogen-deficient $g\text{-}C_3N_4$ and nitrogen-deficient boron-doped $g\text{-}C_3N_4$ as

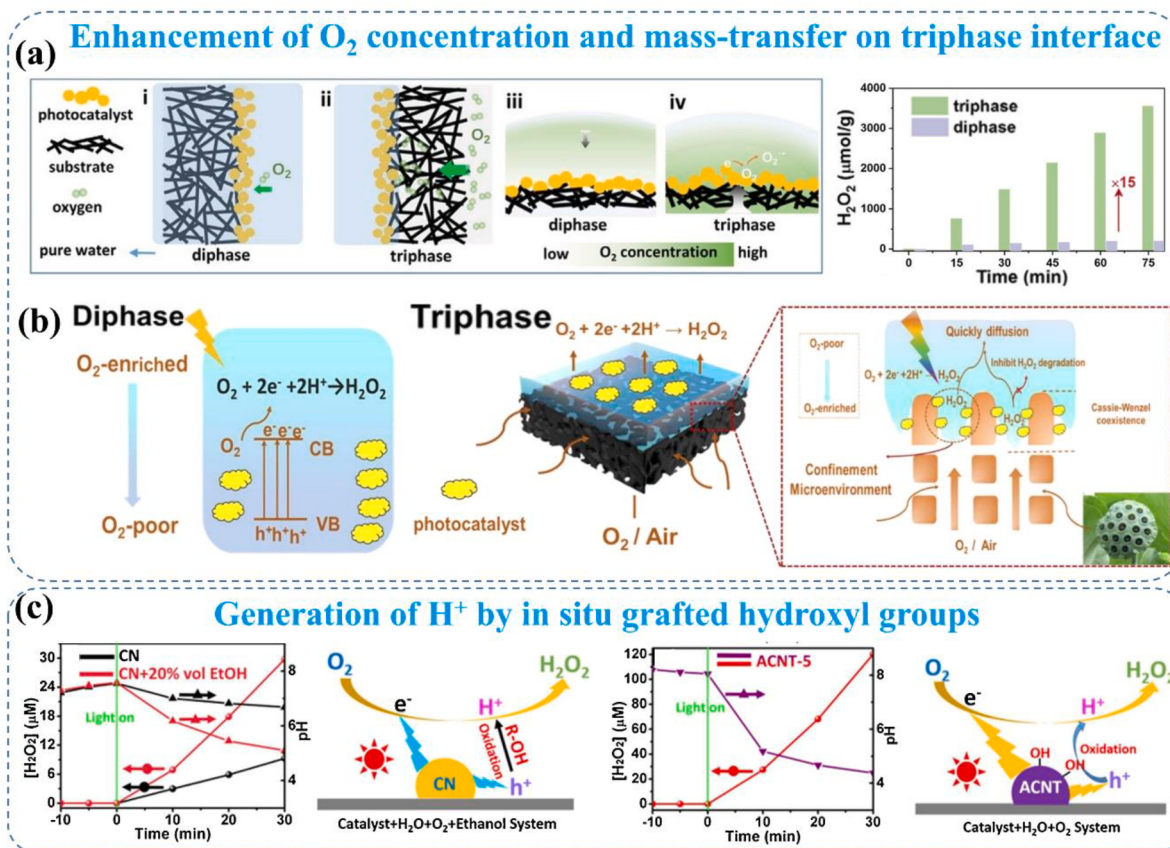


Fig. 5. (a) Schematic illustration and H₂O₂ production of diphase and triphase photocatalytic conditions. Reprinted with permission from [84]. Copyright 2021, John Wiley and Sons. (b) Illustration of triphase interface with tubular confined microenvironment for photocatalytic H₂O₂ generation. Reprinted with permission from [85]. Copyright 2022, Elsevier. (c) Photocatalytic H₂O₂ production and change of pH in CN and alkalized carbon nitride nanotubes (ACNT) systems. Reprinted with permission from [88]. Copyright 2021, Elsevier.

model photocatalysts and forwarded the different reaction mechanisms of active species (¹O₂ and •O₂) with proton donors through experiments and theoretical calculations. The results, shown in Fig. 6b, indicated that the pathways dominated by ROS are more favorable than that dominated by h⁺ due to the lower reaction barrier. Most importantly, the synergistic effect of the water bridge could further decrease the reaction barrier of surface ¹O₂, while it could not act on the pathway dominated by surface free ¹O₂, surface •O₂, and free •O₂. This may be due to the interaction among the proton donor, water bridge, and B site. Therefore, it is vital to continue to explore the reaction mechanisms to provide a theoretical basis for improving the production efficiency of H₂O₂.

In most cases, multiple pathways for ORR coexist in a photocatalytic system and it becomes difficult to determine which reaction pathway is dominant if the CB position of the photocatalyst is without obvious bias. This is because the direct and indirect 2e⁻ ORR are favorable in thermodynamics and kinetics, respectively. However, the undesirable 4e⁻ ORR, which always takes place due to its more positive reaction potential, should be suppressed for its useless product. The selectivity of 2e⁻ ORR on TiO₂ and g-C₃N₄ is achieved through the formation of peroxide species [91,95]. Those organics with condensed aromatic rings, such as rGO, could also act as 2e⁻ ORR active sites via forming 1,4-endoperoxide species [96]. As the most commonly used electron and proton donors, organic alcohols can also improve the selectivity for H₂O₂ by interacting with catalysts and stabilizing the structure of the peroxides. Both H₂O₂ yield and selectivity of TiO₂ in aromatic alcohol were 1 to 2 orders of magnitude higher than that in aliphatic alcohols [95]. Aromatic heterocyclic alcohols demonstrated the same promoting effect on H₂O₂ production [97]. This is mainly because the aromatic rings can stabilize the structure of peroxide on Ti sites by stimulating

electron delocalization. The promoted selective 2e⁻ ORR for H₂O₂ production on TiO₂ in furfural alcohol (FFA) and benzyl alcohol (BA) is presented in Fig. 6c. FFA and BA are capable of forming complexes through deprotonation on TiO₂ surface, which enables the direct hole transfer. The alcohol-oxygen bridge structure can be formed through the combination of molecular oxygen with carbon radical and Ti site. Then, the C—O and O—O bonds dissociate and transform into an aldehyde and peroxide, promoting the 2e⁻ ORR.

Theoretically, the reduction of O₂ to water is inevitably accompanied by the rupture of the O—O bond. Thus, reducing the rupture of the O—O bond can effectively inhibit 4e⁻ ORR and improve the selectivity of 2e⁻ ORR. For example, the selectivity of H₂O₂ production could increase from just 36 % using pristine TiO₂ to 45 %, and to even over 80 % using Pd/TiO₂ and Pd/APTMS/TiO₂ catalysts, respectively owing to the protons accumulation induced by the Pd nanoparticles and surface-anchored organic ligands that promote the protonation of superoxide and inhibit the homolytic O—O bond cleavage on μ-peroxy coordination [82]. Moreover, the activity and selectivity of ORR has been modified by manipulating metallic sites. Recent research showed that the end-on O₂ adsorption configuration (Fig. 6d) of single metal atoms can minimize O—O bond splitting to inhibit unfavorable 4e⁻ ORR. As a result, single metal atom photocatalysts were considered as ideal candidates to boost H₂O₂ production via a highly selective 2e⁻ ORR. Teng et al. [98] dispersed single antimony (Sb) atoms on carbon nitride (Sb-SAPC) for non-sacrificial photocatalytic H₂O₂ synthesis under visible light. The authors observed that the O₂ adsorption configuration of isolated Sb atoms was end-on type, which enhanced the highly selective 2e⁻ ORR by accelerating the formation of Sb-μ-peroxide. In addition to this, the Sb atoms could induce holes to accumulate at the nearby melem units,

Table 2Summary of the reaction condition and pathway of photocatalysts for H₂O₂ production.

Pathway	Photocatalyst	Reaction solution	Light source	Gas	H ₂ O ₂ μmol/h g ⁻¹	CB ^a (eV)	VB ^b (eV)	Ref.
Direct 2e ⁻ ORR	Pd/APTMS/TiO ₂ ^c	100 mM phosphate buffer (pH = 3)	AM 1.5G	–	300	–	–	[82]
	SN-GQD/TiO ₂ ^d	6 % IPA (pH = 2)	Simulated sunlight	–	902	–	–	[70]
	PCNHS ^e	Water	λ > 420 nm	Saturated O ₂	174	–0.80	1.80	[79]
	P-mMCNNs ^f	10 % IPA	Simulated sunlight	Saturated O ₂	1684	–0.32	2.39	[66]
	5 % ethanol	Constant O ₂	1083	–	–	–	–	[66]
	KTTCN ^g	0.5 % IPA	λ > 400 nm	720	–1.72	1.00	[115]	
	PCN-NaCA ^h	3.5 wt% Glycerol	Simulated sunlight	–	18,700	–1.12	1.57	[36]
	ZrS _{1-y} S _{2-x} (15/100)	30 mL H ₂ O with 1 mmol benzylamine	AM 1.5G	–	~ 1500	–0.18	1.8	[61]
	TAPD-(Me) ₂ COF	10 % EtOH	λ = 420–700 nm	Saturated O ₂	97	–0.8	1.83	[116]
	90 % EtOH	Constant O ₂	234.52	–	–	–	–	[116]
Indirect 2e ⁻ ORR	SS-CN ⁱ	10 % IPA	λ > 420 nm	Saturated O ₂	566.69	–1.01	1.78	[65]
	CAN ^j	10 % IPA	λ > 420 nm	Saturated O ₂	174	–0.48	1.87	[117]
2e ⁻ WOR	N ₃ C vacancies carbon nitride	10 % IPA	λ > 420 nm	–	323.6	–0.76	1.89	[81]
	SnO ₂ -coupled cyano modified g-C ₃ N ₄	10 % IPA	λ > 420 nm	–	505.8	–0.77	1.72	[73]
	Ni ₂ P ₂ -CQDs@CdS	Water	λ > 420 nm	Constant O ₂	703.4	–	–	[118]
	g-C ₃ N ₄ -MoS ₂ -Ni(OH) ₂	Water	UV-visible light	–	225	–0.53	1.88	[119]
Dual-channel (2e ⁻ ORR and 4e ⁻ WOR)	Pt/porous brookite TiO ₂ nanoflutes	Water	λ ≥ 300 nm	Anaerobic	300	–0.03	1.79	[100]
	PtO _x -RGO-CN _x	Water	λ = 365 nm	Anaerobic	8200	–0.45	2.76	[120]
	Pt@β-CD/C ₃ N ₄ ⁺ M	Water	λ > 400 nm	Saturated O ₂	275	–0.25	2.63	[86]
	g-C ₃ N ₄ /PDI ^k	Water	λ > 420 nm	Saturated O ₂	147	–0.72	1.81	[92]
	ZnPPc-NBCN ^l	water	λ = 400–800 nm	Saturated O ₂	21	–0.82	1.86	[77]
	Ni-CAT-CN	Water	λ > 420 nm	–	114	–0.69	1.83	[111]
	Sb-SAPC ^m	water	λ > 400 nm	Saturated O ₂	1801	–1.14	1.60	[98]
	PM-CDs ⁿ	Water	λ > 420 nm	–	91.1	–0.71	1.23	[72]
	Ni ₂ P/CDS	Water	λ > 420 nm	–	1776	–0.34	1.65	[62]
	CoO _x /MoBiVO ₄ /Pd	PBS solution (pH = 7.4)	AM 1.5 G	Saturated O ₂	1385.42	–0.27	1.63	[107]
Dual-channel (2e ⁻ ORR and 2e ⁻ WOR)	CTF-BDBBN ^p	Water	λ > 420 nm	Saturated O ₂	9975	–0.2	2.6	[108]
	CDA ^q	Water	λ > 420 nm	–	~ 97	–1.23	1.60	[109]
	HTNT-CD ^r	Water	λ > 365 nm	–	557.2	–0.4	1.97	[71]
	ZIF-8/C ₃ N ₄	Water	λ > 420 nm	–	4240	–	–	[110]
	CPN ^s	Water	λ = 420–700 nm	–	3400	–0.5	2.08	[121]
	Co ₁ /AQ/C ₃ N ₄ ^t	Water	AM 1.5 G	Constant O ₂	1968	–	–	[106]
	CoWO ₄ @Bi ₂ WO ₆	Water (pH = 3)	λ > 420 nm	Saturated O ₂	116	–~53	–0.89	2.77

^a CB represents the position where the ORR takes place on the corresponding semiconductor.^b VB represents the position where the WOR takes place on the corresponding semiconductor.^c APTMS: aminopropyltrimethoxysilane.^d sN-GQD: sulfur and nitrogen co-doped graphene quantum dots.^e PCNHS: P doped g-C₃N₄ with a hollow sphere structure.^f P-mMCNNs: phosphorus-modified macro-mesoporous carbon nitride nanosheets.^g KTTCN: K intercalated tri-s-triazine units.^h PCN-NaCA: polymeric carbon nitride framework with sodium cyanamate moiety.ⁱ SS-CN: sulfur doped g-C₃N₄.^j ACN: 2-hydroxy-4,6-dimethylpyrimidine grafted polymeric carbon nitride.^k PDI: pyromellitic diimide.^l ZnPPc: zinc polyphthalocyanine; NBCN: sodium borohydride modified carbon nitride.^m Sb-SAPC: single Sb atoms dispersed on carbon nitride.ⁿ PM: photocatalyst composed of procyanidins and 4-methoxybenzaldehyd.^o PC-MB: procyanidin-methoxy-benzaldehyde.^p CTF: covalent triazine frameworks; BDBBN: 4,4'-(buta-1,3-diyne-1,4-diy) dibenzonitrile.^q CDA: crosslinking polymer catalyst constructed by β-cyclodextrin aldehyde and 4-amino-6-hydroxy-2-mercaptopurine.^r HTNT: proton-form titania nanotube with carbon dot.

^s CPN: phosphorous doped porous carbon nitride.

^t AQ: anthraquinone.

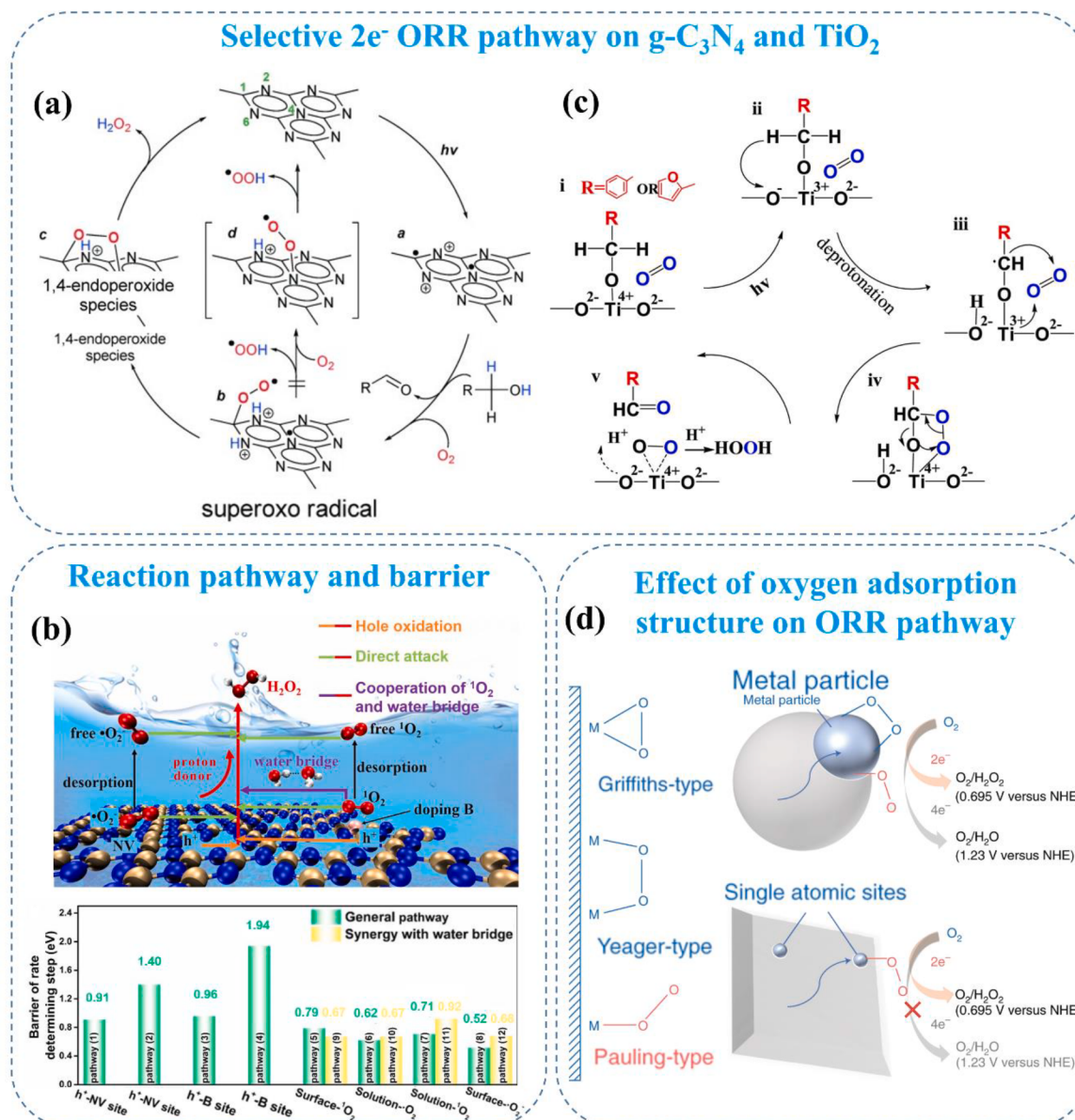


Fig. 6. (a) Proposed mechanism of $\text{g-C}_3\text{N}_4$ for selective H_2O_2 formation. Reprinted with permission from [92]. Copyright 2014, John Wiley and Sons. (b) Schematic of reaction mechanisms on nitrogen-deficient and boron-doped $\text{g-C}_3\text{N}_4$ (NCBN). Reprinted with permission from [94]. Copyright 2022, Elsevier. (c) 2e^- ORR pathway for H_2O_2 formation on TiO_2 in the presence of furfural alcohol or benzyl alcohol. Reprinted with permission from [97]. Copyright 2022, Elsevier. (d) Schematic structures of O_2 adsorption on the metal surface. Reprinted with permission from [98]. Copyright 2021, Springer Nature.

accelerating the 4e^- WOR to produce O_2 and participate in the ORR process. In subsequent research, they developed a series of metal single-atom photocatalysts (M-SAPCs) including two main-group metals (In, Sn) and three transition metal (Fe, Co, Ni) atoms [99]. In a similar manner to their previous study, In-SAPC and Sn-SAPC exhibited higher charge separation and end-on O_2 adsorption configuration that raises the rate of the 2e^- ORR process. Meanwhile, the Fe-SAPC, Co-SAPC, and Ni-SAPC showed higher rate of charge recombination, even resulting in a lower H_2O_2 production rate than pristine PCN. From this, one can obviously see that not all single atom photocatalysts may result in augmented H_2O_2 production and that proper selection of a suitable single-atom catalyst is pivotal and requires an in-depth research endeavor in the future so as to maximize the yield.

Concerning WOR, H_2O_2 was mostly investigated as a valuable

byproduct in photocatalytic water splitting for H_2 gas production [100–103]. Cao *et al.* [100] reported Pt/porous brookite TiO_2 nanoflakes for the production of H_2 and H_2O_2 from pure water through the two-electron photocatalytic intermediate water splitting (PIWS) mechanism. The production rates of H_2O_2 and H_2 were >12 times and 230 times than reported $\text{H}_2/\text{H}_2\text{O}_2$ production systems through photocatalytic overall water splitting (POWS) due to the lower reaction barrier (Fig. 7a). Wei *et al.* [102] synthesized Cu NPs modified TiO_2 hollow spheres through three steps for photocatalytic water splitting. Interestingly, they found that different redox active sites under different irradiation wavelengths led to the selectivity of WOR products (H_2O_2 under UV light and O_2 under visible light, Fig. 7b). In fact, the VB position of many photocatalysts in previous studies could meet the reaction potential of WOR, but some researchers ignored this process due likely to

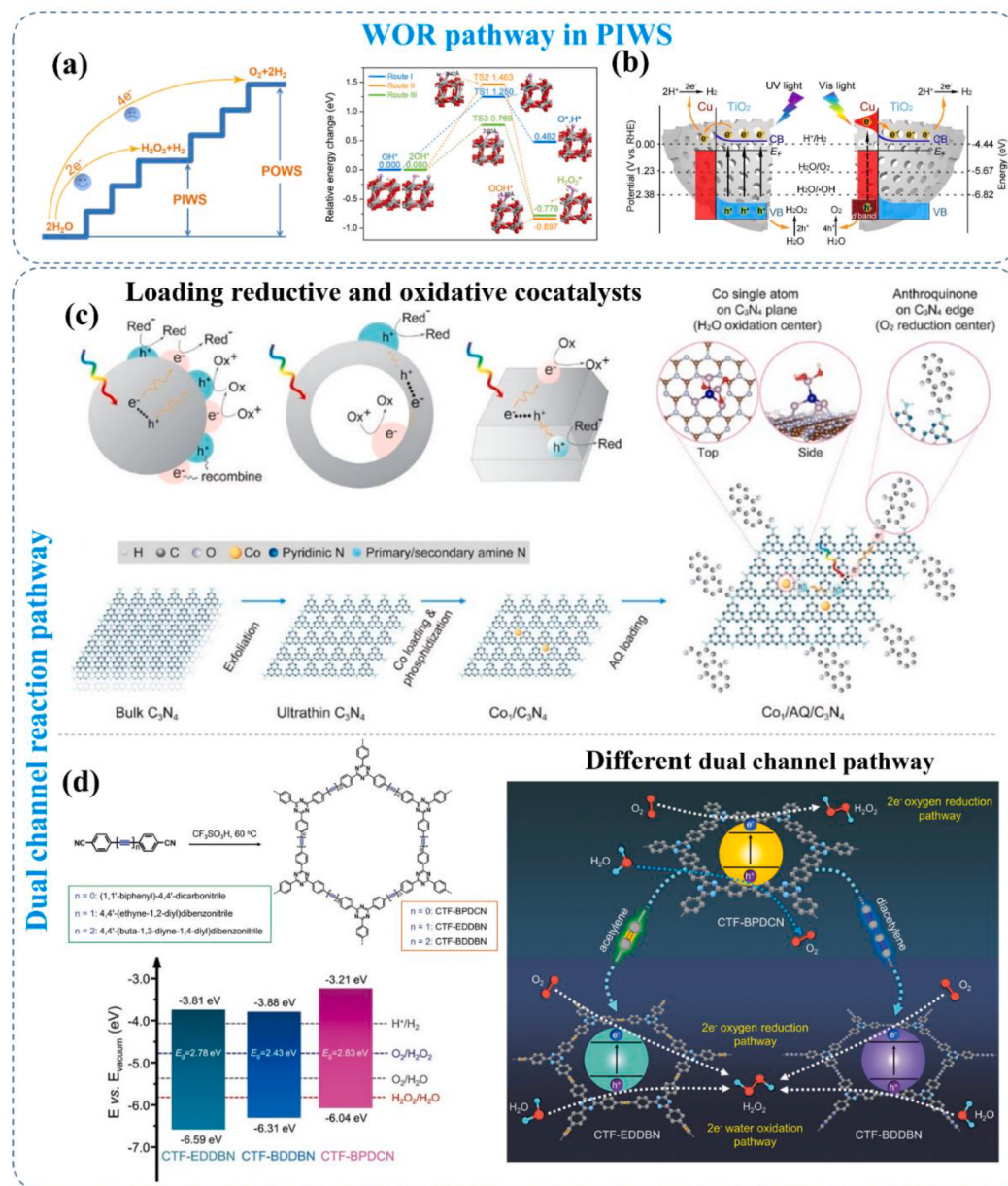


Fig. 7. (a) Calculated energy profile of intermediate water splitting (PIWS) on Pt/porous brookite TiO_2 . Reprinted with permission from [100]. Copyright 2020, Elsevier. (b) Mechanism illustration. Reprinted with permission from [102]. Copyright 2020, Elsevier. (c) Spatial separation of Co single atom (as oxidation center) and anthraquinone (AQ, as reduction center) cocatalysts on C_3N_4 . Reprinted with permission from [106]. Copyright 2022, National Academy of Science. (d) Schematic illustration of electronic band structures and reaction pathways of different covalent triazine frameworks (CTFs) for H_2O_2 production. Reprinted with permission from [108]. Copyright 2019 John Wiley and Sons.

the insufficient oxidation capacity and slow kinetics. With the increasing focus on photocatalytic H_2O_2 production from pure water without sacrificing agents, researchers began to shift their attention away from simple ORR toward integrated dual-channel reactions.

As mentioned earlier, the dual-channel reaction is an ideal pathway for H_2O_2 production because of the mutual promotion between ORR and WOR through additional H^+ or O_2 reactants supply and full utilization of electron-hole pairs. Tuning the CB and VB position of the employed photocatalysts to meet the reaction position of ORR and WOR is the precondition for integrating the dual channel. $\text{g-C}_3\text{N}_4$ demonstrated superior activity towards ORR by virtue of its special reaction pathway, but its WOR activity response was unfavourable due to its low VB position. To alleviate this problem, various electron-deficient groups such as pyromellitic diimide (PDI) [92], biphenyl diimide (BDI) [104], and mellitic triimide (MTI) [105] were introduced to tune the VB position for

higher WOR activity while retaining sufficient ORR capacity to achieve the dual-channel H_2O_2 production. Although the addition of these organic groups may also cause a slight extension in the bandgap, they gave rise to higher H_2O_2 yield due to their greater ORR and WOR activities. Moreover, loading reductive and oxidative cocatalysts on a photocatalyst as oxygen reduction and water oxidation centers is an espoused strategy to integrate ORR and WOR. Chu *et al.* [106] anchored Co single atoms (Co_1) and AQ as cocatalysts to the void center and the edge of the C_3N_4 respectively (Fig. 7c) to effect efficient H_2O_2 production. This spatial separation of Co_1 and AQ on C_3N_4 ensured the functionality of both of them as cocatalysts. The Co_1 enhanced the WOR activity because of its strong water adsorption and mid-gap states, promoting charge separation, whereas the AQ enhanced H_2O_2 production selectivity through a two-step reaction of reductive hydrogenation and dehydrogenation between it and hydroxyanthraquinone (AQH_2).

Liu and co-authors [107] selectively loaded CoOx and Pd on the {110} and {010} facets of Mo₃BiVO₄ as WOR and ORR cocatalysts, respectively, and they found H₂O₂ production rate of 9975 μmol g⁻¹ h⁻¹, which is the highest value for inorganic semiconductor catalysts. In addition, some other photocatalysts with suitable bandgap positions can also produce H₂O₂ via such a dual-channel pathway. To give a specific example, Chen *et al.* [108] reported three kinds of covalent triazine frameworks (CTFs) achieving the integration of 2e⁻ ORR and 2e⁻/4e⁻ WOR for H₂O₂ production, as illustrated in Fig. 7d. The introduction of acetylene (-C≡C-) and diacetylene (-C≡C-C≡C-) moieties to CTFs (CFT-EDDBN and CTF-BDDBN) enhanced their oxidation capability and reduced the energy of OH* formation, enabling the 2e⁻ WOR pathway to produce H₂O₂. As reported in our previous study [109], a crosslinking polymer catalyst constructed by β-cyclodextrin aldehyde and 4-amino-6-hydroxy-2-mercaptopurimidine also achieved outstanding H₂O₂ yield over a wide pH range of 1–11 without electron donor and oxygen aeration, and this is ascribed to the mutual promotion of ORR and WOR.

However, photocatalysts with sufficient reaction potentials for ORR and WOR usually possess broad bandgaps, which may cause light absorption to be a new limiting factor. Additionally, it is difficult to design a novel photocatalyst with defined CB and VB positions. Therefore, utilizing two types of semiconductors to construct heterojunctions with higher reduction and oxidation potentials is a more commonly used approach to effect dual-channel H₂O₂ production. Zhao *et al.* attempted different types of MOFs such as ZIF-8 [110] and Ni-CAT [111] to construct a heterojunction with C₃N₄. The large surface area and abundant microporous structure of MOFs were conducive to providing more active sites, improving the oxygen adsorption as well as accelerating the mass transfer and diffusion. The obtained results showed that the H₂O₂ production efficiency utilizing the ZIF-8/C₃N₄ composite catalyst reached 2641 μmol h⁻¹ g⁻¹ without sacrificial agents at normal pressure under visible light irradiation, and the Ni-CAT-CN produced a rate of 1801 μmol g⁻¹ h⁻¹. Additionally, other heterojunctions based on CN with various semiconductors such as Bi₄O₅Br₂ [112], perylene imides (PI) [113], hexagonal boron nitride (h-BN) [114] have proved effective in the production of H₂O₂ through the same dual-channel mechanistic pathway. Although these heterojunctions could give rise

to higher yields than their corresponding single components via such a pathway, the difference between their yields is still very large. Therefore, the effects of the other steps described previously on their rate of formation need also to be taken into consideration.

3.3.3. Stabilization and separation of products

The final crucial step in the photocatalytic H₂O₂ production is the stabilization and separation of the product. If the produced H₂O₂ cannot be effectively separated from the photocatalysts, it may undergo in situ decomposition on the surface of the catalysts. Additionally, the catalysts may be poisoned by H₂O₂, which will also affect the yield and subsequent production efficiency. The influence of typical modification strategies on the generation and decomposition of H₂O₂ is shown in Table 3. Although some of the aforementioned modification strategies can effectively improve production efficiency, they may also at the same time promote the decomposition of H₂O₂ to a certain extent, and thus, it is essential to find a balance between the formation and decomposition of H₂O₂ to maximize production.

Among the strategies specified, the effect of noble metal loading is most noticeable, and is usually related to the type, quantity, and size of the loaded noble metals. For example, the decomposition rate of H₂O₂ usually increases with increase in the loading quantity of noble metals, such as Au or Ag [54,122], and that the enhanced rate of decomposition in the presence of Pd metal was ascribed to the low energy barrier and the sensitive scission of O—O bond to Pd surface structure [123,124]. As a well-known catalyst with high activity for H₂O₂ degradation, the decomposition rate constant (k_d) of Pt/TiO₂ was found to be more than twice that of Au/TiO₂ [125]. This makes Au to be more suitable to be loaded on TiO₂ surface to effect higher synthesis while lowering decomposition, and the effect may be further optimized by changing its size (Fig. 8a). Wang *et al.* [122] also found that the order of k_f and k_d values of various noble metals loading on WO₃ was Pd > Au > Pt > Ag and Pt > Pd > Ag > Au, respectively. Therefore, the difference between various noble metals makes it possible to increase the k_f and decrease the k_d values simultaneously under their synergistic effect. Taking Au-Ag alloy as an example, the Au with higher electronegativity would attract electrons from Ag, resulting in the reduced and increased affinity

Table 3
Summary of strategies for stabilizing H₂O₂ on photocatalysts surface.

Strategy	Photocatalyst	Light source	Reaction solution	Reaction time/h	Before modification			After modification			Ref.	
					$k_f/\text{mM h}^{-1}$	k_d/h^{-1}	[H ₂ O ₂]/mM	$k_f/\text{mM h}^{-1 \text{a}}$	$k_d/\text{h}^{-1 \text{b}}$	[H ₂ O ₂]/mM		
Noble metal loading (type and size)	Au/TiO ₂	2.1 nm 7.7 nm 12.5 nm	λ > 300 nm	4 % methanol	6	0.45	1.02	0.4	1.75 1.37 1.25	0.42 0.25 0.24	3.8 4.2 4.0	[125]
	Au/WO ₃		λ > 420 nm	4 % methanol	5	–	–	0.0085	0.167 0.199 0.086 0.092	0.22 0.64 0.46 1.02	0.523 0.312 0.171 0.0909	[122]
	Pd/WO ₃								0.32	0.26	1.2	
	Ag/WO ₃								0.15	0.12	1.0	
	Pt/WO ₃											
	Au _{0.1} Ag _{0.4} /TiO ₂		λ > 280 nm	4 % ethanol	12	0.18	0.34	0.5	0.57 0.32 0.15	0.14 0.26 0.12	3.4 1.2 1.0	[126]
	Au _{0.1} TiO ₂											
Surface passivation and hydrophobic modification	Ag _{0.4} /TiO ₂											
	rGO/TiO ₂ /P		λ > 300 nm	5 % 2-propanol (pH = 3)	3	1.26	0.025	0.83	2.1	0.24	4.5	[127]
Two-phase system	CdS@S-doped carbon		λ > 420 nm	20 % 2-propanol	3	0.348	0.468	0.56	1.314	0.204	2.95	[129]
	PF2FBT/TiO ₂ ^c		λ > 350 nm	Water	2	0	15	0	0.09	0.03	0.18	[130]
	MIL-125-R7		λ > 420 nm	5.0 mL benzyl alcohol and 2.0 mL water	3	–	–	~0.3	–	–	~15	[131]
	OPA/MIL-125- NH ₂ ^d					–	–	~0.5	–	–	~6.5	[132]
	OPA/Zr _{92.5} Ti _{7.5} - MOF					–	–	~1.5	–	–	~30	[133]
	OPA/Fe-Zr-MOF								~5		~40	[134]

^a k_f : formation rate constant.

^b k_d : decomposition rate constant.

^c PF2FBT: poly(9,9-diethyl fluorine-*alt*-difluorobenzothiadiazole).

^d OPA: octadecylphosphonic acid.

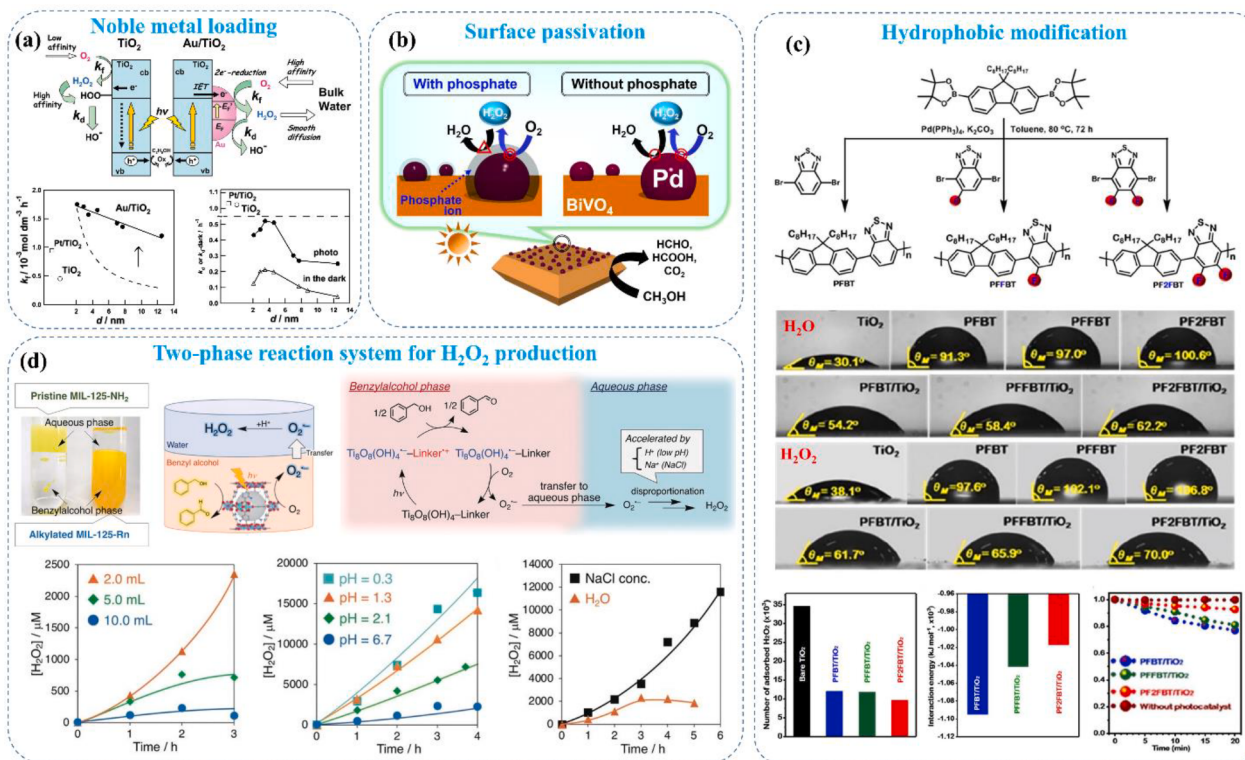


Fig. 8. (a) Synthesis and decomposition of H_2O_2 on Au/TiO_2 . Reprinted with permission from [125]. Copyright 2010 American Chemical Society. (b) Proposed mechanism of phosphate ion-coated $\text{Pd}-\text{BiVO}_4$ for photocatalytic H_2O_2 production. Reprinted with permission from [128]. Copyright 2020, Elsevier. (c) The hydrophobicity and its effect on H_2O_2 adsorption and decomposition. Reprinted with permission from [130]. Copyright 2021, Elsevier. (d) Schematic illustration and yield of H_2O_2 production in two-phase reaction system. Reprinted with permission from [131]. Copyright 2019, John Wiley and Sons.

of the former and the later metals for H_2O_2 , respectively [126]. Thus, higher values of k_f and lower k_d could be achieved by adjusting the ratio of Ag and Au in the alloy.

Surface passivation is another potential strategy that could be adopted to retard the undesirable decomposition of H_2O_2 . As a widely known H_2O_2 stabilizer, phosphate can be used as a surface passivation agent on photocatalysts to inhibit H_2O_2 adsorption and decomposition (Fig. 8b) [127,128]. Modifying the hydrophobicity of a photocatalyst can also minimize the adsorption and decomposition rates by passivating its surface. Lee *et al.* [129] utilized the hydrophobic property of sulfur-doped carbon nanocomposites to prevent the adsorption and decomposition of H_2O_2 on the CdS catalyst. Uncommonly, the surface passivation effect of CdS in KOH solution makes the concentration of H_2O_2 under alkaline conditions much higher than that under acidic and neutral conditions, and the authors found 17.1 mM final H_2O_2 concentration in KOH solution under visible light with 2-propanol used as a sacrificial agent. In a different study, Hong *et al.* [130] first utilized visible light responsive fluorinated polymers (PFBT, PFFBT, and PF2FBT) to construct heterostructures with TiO_2 (Fig. 8c) that decreased the adsorption and in-situ destruction of H_2O_2 on the photocatalysts. The H_2O_2 adsorption affinity of the polymer/ TiO_2 was declined through the hydrogen bonds formed between it and the N atoms of the fluorinated polymers and its interaction with dangling Ti and bridge O atoms.

Furthermore, hydrophobic materials can achieve complete H_2O_2 separation in a two-phase photocatalytic system. Yamashita research group developed a series of hydrophobic MOFs for H_2O_2 production in the two-phase system, achieving the spatial separation of H_2O_2 in the aqueous phase and MOFs in the BA phase [131–134]. The hydrophobic MIL-125-Rn, which was synthesized by grafting MIL-125-NH₂ with various alkyl chains, was selectively dispersed in the BA phase instead of the aqueous phase (Fig. 8d), and the two-phase system helped to realize not only the spontaneous separation of H_2O_2 and benzaldehyde but also

obtain high concentration of H_2O_2 by reducing the volume of the aqueous phase. The two-phase system also makes it possible to synthesize H_2O_2 rapidly at a very low pH of 0.3, where MIL-125-NH₂ would dissolve in few seconds.

In this section, the surface reactions for H_2O_2 production are discussed from three aspects. Firstly, improving the utilization of oxygen through enhanced absorption is limited by its solubility in the liquid phase, while providing sufficient O_2 or H^+ for ORR through WOR is a preferred strategy. Although some photocatalysts meet the bandgap requirement of the dual-channel reaction pathway, most studies only explored their ORR route and ignored the WOR pathway due likely to the utilization of sacrificial agents. Therefore, subsequent research should pay more attention to the design of dual-channel photocatalysts to improve their application under natural conditions without sacrificial agent, oxygen aeration, and pH adjustment. Moreover, the reaction mechanism involving complex ROS conversion needs to be clarified through rigorous and scientific methods. Finally, the issue of decomposition on catalyst surface should be kept in mind, and that appropriate design strategies must be adopted to increase H_2O_2 generation while avoiding its decomposition.

4. Environmental applications

As the most commonly used oxidant, H_2O_2 is widely used in environmental applications. According to the requirement of oxidation capacity, it is usually utilized through direct application or Fenton reaction. In this section, we summarize the applications of in-situ photocatalytic H_2O_2 production in disinfection and pollutant degradation.

4.1. Disinfection

Compared with commonly used chlorine disinfection, H_2O_2 can

inactivate bacteria without producing disinfection byproducts. Photocatalytic H₂O₂ production system can produce H₂O₂ on site and on demand, which is more convenient and safer than chlorine disinfection. Currently, one of the major limitations of photocatalytic H₂O₂ production-based disinfection is that the disinfection efficiency is lower than that of chlorine disinfection due to the unsatisfactory H₂O₂ production yield. Therefore, strategies need be adopted to enhance the H₂O₂ production yield.

It is generally assumed that the main mechanism of photocatalytic disinfection is to attack bacteria through ROS (H₂O₂, •O₂ and •OH), then destroy their physiological structure, antioxidant enzyme system, respiratory system, and metabolic system that are closely related to their survival (Fig. 9). H₂O₂ as the unique stable molecule ROS in water is more efficient for bacteria inactivation than other ROS with a very short lifetime which can only diffuse a very short distance and inactive the pathogens close to the photocatalyst [135]. Bacteria can be efficiently inactivated by several μM levels of H₂O₂ [136–141], which can be easily produced by most photocatalysts (Table 4). However, different ROS will inevitably transform and cooperate throughout the process. For example, Geng *et al.* [142] found that the H₂O₂ produced in situ on the surface of ZnO/g-C₃N₄ can convert into •OH by the excitation of sunlight to inactivate *E. coli* and mycete. Besides, ROS will cause damage to iron-storage proteins in bacteria and extract iron from them. The [4Fe-4S]²⁺ cluster would be oxidized to unstable [4Fe-4S]³⁺, then released ferrous iron and [3Fe-4S]⁺ [143]. Thus the internal Fenton reaction between H₂O₂ and Fe²⁺ can facilitate the inactivation process.

Normally, bacteria would not become inactivated when exposed to low concentrate ROS for a short time due to their ROS defense mechanisms (Fig. 9). The most known defense regulators are catalase (CAT) and superoxide dismutase (SOD), which can decompose the H₂O₂ and dismutate •O₂, respectively. Thus, the inactivation rate of bacteria is generally slow in the initial disinfection process, then ROS accumulates in the bacteria until it exceeds the limit of the antioxidant enzyme system. With the decrease of antioxidant enzyme activities such as CAT and SOD, a series of oxidative damage began to appear. Oxidative damage caused by H₂O₂ usually appears first on the cell membrane, then polysaccharides and proteins are broken down. Thus those functions that they're responsible for including ion transport, ATP synthesis, and metabolism have gradually been destroyed. The leakage of ions usually accompanies the whole photocatalytic process, implying the inactivation of Na⁺-K⁺ pumps and the loss of selection permeability of cell membranes. The break of the membrane will affect the electron transport chains of the respiration system, resulting in the protons and redox potential for ATP synthesis cannot be provided. Then, lipid peroxidation (LPO) caused by ROS would fragmentate and rearrange the phospholipid bilayer, which will eventually induce irreversible damage to the

integrity and functionality of the cell membrane. Generally, gram-positive bacteria with only one phospholipid bilayer are more easily inactivated by H₂O₂ than gram-negative bacteria with dual phospholipid bilayer [141,144]. Finally, the leakage and degradation of genetic material which can make them regrow declare the complete death of bacteria.

To further develop the practical application of photocatalytic disinfection, Teng *et al.* [137] fixed the edge-functionalized C₃N₄ onto plastic membrane bags for portable drinkable water production in extreme conditions. It can meet the drinkable water standard of China under solar light irradiation with 1 h and provide about 10 L of purified water which meets the need of four adults per day in 40 times cycle. Moreover, they fabricated a fixed-bed reactor with this photocatalyst for the disinfection of flowing water. Besides, some synergistic methods can further improve the disinfection efficiency and practicability by photocatalytic produced H₂O₂. Photothermal synergistic catalysis combines the advantage of photocatalysis and thermal catalysis. Some photocatalysts, such as CuO₂ loaded WS₂ nanoflowers (CP@WS₂ NFs) [145], Ti₃C₂T_x [146], and WO_{3-x}/C nanosheet [147], can transform near-infrared light to thermal energy and heat the bacterial liquid to nearly 50 °C, which caused the denaturation of proteins and the destruction of bacterial cell membranes. Coupling with the micro/nano bubbles (MNBs) process is another efficient strategy to improve the disinfection efficiency [148]. The supersaturation and sustainable diffusion of O₂ due to the MNBs increased the O₂ supply for H₂O₂ production. Moreover, MNBs enhanced the scattering of light prolonging the length of optical paths in the suspension. Heterogeneity of the electric field enhances the light intensity at the bubble-solution interface. Thus it can improve the light absorption and promote the photocatalytic reactions in this synergetic system for disinfection. Recently, some photocatalysts with an interesting photocatalytic “memory” effect intrigued researchers. Mo-doped TiO₂ could produce 2.59 μM H₂O₂ in the dark after 8 h irradiation of UV light and could inactivate about 50 % of *E. coli* in dark [149]. The electrons can be excited by UV light and part is trapped on the shallow defect level of Mo (Mo⁶⁺ → Mo⁵⁺), which will be released (Mo⁵⁺ → Mo⁶⁺) and reduce O₂ to H₂O₂ in dark. Although the concentration of H₂O₂ produced by the memory effect of the photocatalyst in the dark is still relatively low, it shows us the possibility of photocatalytic disinfection in the special situation without sunlight and maintaining the disinfection effect in dark.

4.2. Pollutant degradation

It has been proved that in situ photocatalytic production of H₂O₂ is an efficient strategy to remove various pollutants including dyestuff, phenols, pharmaceutical and personal care products (PPCPs), and volatile organic compounds (VOCs) (Table 5). However, degrading, especially mineralizing, organic pollutants generally require higher oxidation capacity than that in disinfection. Thus Fenton or Fenton-like process with the in situ production of H₂O₂ was usually applied to improve degradation efficiency. The mechanisms of photocatalytic H₂O₂ production for pollutants degradation in different systems are shown in Fig. 10.

The discharge of printing and dyeing wastewater into the water environment not only causes water color change but also blocks sunlight and reduces the reoxidation of water, causing the death of aquatic creatures. Common dyestuff including rhodamine B (RhB), methylene blue (MB), and methyl orange (MO) can all be decolorized under the action of continuously generated H₂O₂. The degradation rate of dyes usually depends on H₂O₂ productivity and the molecule structure of target. That is why RhB with more complex molecules containing aniline, carboxyl, and N⁺ groups required higher energy and more H₂O₂ to degrade the intermediates than MB [152]. Notably, the intermediate •OH and •O₂ generated in WOR and ORR during the photocatalytic H₂O₂ production process and the h⁺ retained in photocatalyst will inevitably participate in the degradation reaction. Besides, the in situ

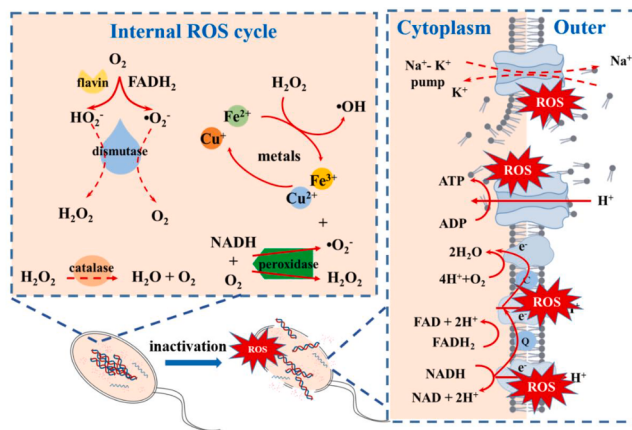


Fig. 9. Internal ROS cycle of bacteria and schematic illustration of the anti-bacterial activities of the ROS.

Table 4Summary of photocatalytic disinfection with H₂O₂ as dominant reactive species.

Catalyst	Bacteria	Light source	Catalyst dosage	Time	Inactivation performance	Dominant reactive species	H ₂ O ₂ yield (μM h ⁻¹)	Ref.
g-C ₃ N ₄ /TiO ₂	<i>E. coli</i> 10 ³ CFU/mL	Simulated sunlight	0.1 g/L	30 min	96.8 %	H ₂ O ₂ , •O ₂ ⁻	~1.2	[136]
edge-functionalized g-C ₃ N ₄ film	<i>E. coli</i> 10 ³ CFU/mL	λ > 400 nm	5 cm ² film 10 mg/L	30 min	6 log	H ₂ O ₂ , •O ₂ ⁻	~6	[137]
Amino-rich porous ultrathin g-C ₃ N ₄ nanosheets	<i>E. coli</i> 3 × 10 ⁸ CFU/mL λ > 400 nm	AM 1.5 G	1 g/L	30 min 120 min	14.96 log/h 3.74 log/h	H ₂ O ₂	~10	[150]
Polyethylenimine grafted C ₃ N ₄	<i>E. coli</i> , <i>E. faecalis</i> 10 ³ CFU/mL	Simulated sunlight	1 g/L	45 min 60 min	6.2 log 4.2 log	H ₂ O ₂ , •O ₂ ⁻	63.2	[151]
ZnO/g-C ₃ N ₄	<i>E. coli</i> , etc	320 nm < λ < 780 nm	1 g/L	60 min	97.4 %	•O ₂ ⁻ , •OH	664 (10 % IPA, pH = 3) ~1.9	[142]
g-C ₃ N ₄ /monoclinic Bi ₂ O ₄	<i>E. coli</i> 6log ₁₀ CFU/mL	λ > 400 nm	0.4 g/L	1.5 h	6 log ₁₀	H ₂ O ₂ , h ⁺		[138]
1 T-rich MoS ₂ /g-C ₃ N ₄	<i>E. coli</i> 2 × 10 ³ CFU/mL	Simulated sunlight	0.1 g/L	60 min	100 %	H ₂ O ₂	8.6	[139]
FLV-MoS ₂ ^a	<i>E. coli</i> 10 ⁵ CFU/mL	Simulated sunlight	1.6 mg/L	20 min	>99.999 %	H ₂ O ₂	~2.5	[140]
Natural sphalerite	<i>E. coli</i> <i>M. barkeri</i> 1.5 × 10 ⁷ CFU/mL	λ > 400 nm	1 g/L	3 h 10 h	100 % (pH = 10)	H ₂ O ₂	several μM	[141]
Ag/TiO ₂ with MNBs ^b	<i>B. subtilis</i> 10 ⁵ CFU/mL	λ > 420 nm	1 g/L	60 min	66.6 %	H ₂ O ₂	–	[148]
Mo-doped TiO ₂	<i>E. coli</i> 10 ⁷ CFU/mL	UV light (8 h)	1.67 g/L	4 h (dark)	~50 %	H ₂ O ₂	~35.2 (UV) ~2.59 (dark)	[149]

^a FLV: few-layered vertically aligned.^b MNBs: micro/nano bubbles.

Fenton or Fenton-like process may occur during the reaction. Song *et al.* [152] have found that separated reaction solution (6 h) of Au@MoS₂ failed to decolorize the MB which can be decolorized immediately after Fe²⁺ adding, exhibiting the efficiency of the in situ Fenton process. Except for Fe, Mn [153] and Au [152] have also been proved to be Fenton-like centers, which can transform H₂O₂ generated in situ into •OH to participate in the degradation of dyestuff (Table 5).

Phenolic compounds are typical toxic organic pollutants, which are harmful to human health and aquatic creature. The photo-Fenton with in situ generated H₂O₂ has been reported to be an efficient strategy for degrading a series of phenolic compounds, such as phenol, chlorophenol, nitrophenol, gallic acid, bisphenol A, and benzoic acid [154–159]. Torres-Pinto *et al.* [154] have reported an exfoliated g-C₃N₄ to degrade the mixture of four phenolic compounds. The results showed that the mineralization rate of the mixture with 1 ppm Fe²⁺ increased about 20 % more than that without Fe²⁺. Notably, the mineralization rate in the pure photocatalytic system without Fe²⁺ was nearly-five times that in the traditional Fenton system (1 ppm Fe²⁺ and 2.5 mM H₂O₂), which confirmed the superiority of in situ photocatalytic H₂O₂ production. Similarly, the research of Ma *et al.* [155] showed a great increase in degradation and mineralization of 2,4-dichlorophenol and a decrease in the consumption of Fe²⁺ in the photocatalysis-self-Fenton system than that in the traditional Fenton system. Another advantage of Fenton reaction with in situ generated H₂O₂ is that it can work at natural pH or even alkaline conditions [156], which is the limiting factor for traditional Fenton reaction. Furthermore, some Fe-based photocatalysts have been developed for in situ H₂O₂ production and in situ Fenton reaction to avoid the slow and complex mass transfer process in the traditional Fenton reaction. Zhang *et al.* [157] have embedded CDots onto the surface of FeOCl as the reactive sites for effective separation of electrons and holes, which changed its ORR pathway to produce H₂O₂ instead of •O₂⁻. The Fe³⁺ on the surface of FeOCl would be converted to Fe²⁺ by part of the excited electrons, and then rapidly activate the H₂O₂ to produce abundant •OH through the classical Fenton process. The

oxidation efficiency and mineralization rate of p-chlorophenol in this system were about 4 and 6 times higher than that of FeOCl alone. Moreover, constructing photocatalysts with magnetite, such as Fe₃O₄, and NiFe₂O₄ can not only provide Fe²⁺/Fe³⁺ for the in-situ Fenton reaction but also achieve the separation and recycling of photocatalysts [158,160].

PPCPs are emerging pollutants, which have posed serious threats to human health and aquatic creature. Similarly, PPCPs can be degraded by the •OH produced by the in situ Fenton reaction, and some of the aforementioned photocatalysts can also be effective for the degradation of PPCPs, such as sulfamethoxazole and ciprofloxacin [155]. Besides, many researchers have focused on developing novel photocatalysts for the production of H₂O₂ and degradation of PPCPs simultaneously [69,113,155,161,162]. However, most of them may be double functional photocatalysts rather than utilized generated H₂O₂ to degrade the pollutants. In these reaction processes, •O₂⁻, •OH, and H⁺ have usually been determined as the main oxidation species through quenching experiments [69,161,162], which could not exclude the effect of the inhibition of H₂O₂ production and the conversion between different ROS. Therefore, the exact interactional mechanism between H₂O₂ production and PPCPs degradation still needs to be explored. Wang *et al.* [163] investigated the generation and conversion pathway of H₂O₂ and •OH on the crystalline graphitic carbon nitride (GCN) with condensed tri-triazine structures. The results show that •OH cannot generate on its VB due to its more negative VB position than that of •OH/H₂O. It generates H₂O₂ through the one-step two-electron ORR pathway, then produced •OH via the decomposition of H₂O₂. Naproxen was hydroxylated, decarboxylated, and demethoxylated under the attack by •OH. Moreover, they detected the degradation rate in the real wastewater and mixed PPCPs pollutants solution, which shows the potential of photocatalytic H₂O₂ production for the treatment of PPCPs.

Arsenic (As) pollution in groundwater and soil is a threatening environmental problem. Photocatalytic H₂O₂ production also showed good potential in the oxidation treatment of Arsenic (As) pollution.

Table 5Photocatalytic production of H₂O₂ for pollutant degradation.

Catalyst	Contaminant	Pollutant volume/concentration	Light source	pH	Catalyst dosage	H ₂ O ₂ yield (μM h ⁻¹)	Fenton types	Degradation efficiency	Rate constant k (min ⁻¹)	Ref.
BP/CN	RhB	80 mL/10 ⁻⁵ M	λ > 400 nm	–	20 mg	900 (10 % IPA)	–	98 %/15 min	0.288	[169]
Mn ₃ O ₄ /Co ₉ S ₈	MB	50 mL/2 × 10 ⁻⁵ M	Visible light	–	50 mg	~1000	In-situ	~95 %/40 min ~92 %/ 180 min	–	[153]
Au(0.50)@Mn/MoS ₂	MB	100 mL/2 × 10 ⁻⁵ M	Visible light	9	50 mg	~500	In-situ	100 %/60 min ~75 %/ 120 min	0.01451	[152]
Ag@U-g-C ₃ N ₄ -NS	MB	50 mL/10 mg L ⁻¹	AM 1.5G	–	25 mg	~70	–	88.5 %/40 min 89 %/80 min	–	[54]
Exfoliated g-C ₃ N ₄	Phenol	0.64 mM	LED	6.1	1 g/L	~1500	–	100 %/ 180 min	–	[154]
P doped g-C ₃ N ₄	2,4-dichlorophenol	30 mL/20 mg L ⁻¹	λ > 420 nm	6.4	30 mg	~50	10 mg Fe ²⁺	~95 %/3h	0.712	[155]
Garland g-C ₃ N ₄	2,4-dichlorophenol	50 mL/5 mg L ⁻¹	λ > 420 nm	–	25 mg	~10	5 mg Fe ²⁺	88.8 %/30 min	0.070	[159]
CdS/rGO	Phenol	20 mL/10 mg L ⁻¹	λ > 420 nm	–	20 mg	290.34	1.8 mM Fe ²⁺	100 %/60 min	–	[156]
FeOCl/CDots	p-chlorophenol	100 mL/5 mg L ⁻¹	Visible light	–	100 mg	112.4	In-situ	90.1 %/ 180 min	0.012	[157]
ZnO@Fe ₃ O ₄	p-nitrophenol	200 mL/35 mg L ⁻¹	λ = 400–1700 nm	3	50 mg	788	In-situ	100 %/60 min	0.0213	[158]
Ag ₃ PO ₄ @NiFe ₂ O ₄	MO	80 mL/10 mg L ⁻¹	λ > 420 nm	–	20 mg	~160	In-situ	96.8 %/30 min ~100 %/ 30 min	0.12	[160]
CoWO ₄ @Bi ₂ WO ₆	CIP ^a	50 mL/10 mg L ⁻¹	λ > 420 nm	–	40 mg	~50	–	84.6 %/ 180 min	0.00839	[113]
	ENR ^b								0.00939	
	LOM ^c								0.00656	
BNQD/UPCN ^d	Oxytetracycline hydrochloride	50 mL/10 mg L ⁻¹	λ > 420 nm	–	50 mg	72.30 (10 % IPA)	–	82 %/60 min	0.0309	[69]
CeO ₂ /g-C ₃ N ₄ (VI)	TetracyclineCr	100 mL/10 mg L ⁻¹	λ > 420 nm	–	15 mg	~150 μM	–	78.90 %/ 60 min	0.0320	[161]
20 mg						(10 % IPA)				
CN/rGO@BPQDs ^e	Tetracycline RhB	100 mL/50 mg L ⁻¹	λ = 420–800 nm	–	100 mg	60	–	95 %/150 min 97 %/20 min	0.0194 0.183	[162]
		100 mL/10 mg L ⁻¹								
Crystalline carbon nitrides	Naproxen	50 mL/8 mg L ⁻¹	λ > 420 nm	–	50 mg	~3.5	–	98.4 %/70 min	~0.03	[163]
mCN/WO ₃	As(III)	40 mL/500 μM	λ > 420 nm	3	40 mg	~70	70 μM Fe ³⁺	100 %/90 min	–	[164]
FeS ₂ -RFR ^f	Roxarsone	50 mL/20 mg L ⁻¹	AM 1.5G	4.8	50 mg	400	In-situ	100 %/ 120 min	0.03107	[165]
PI-g-C ₃ N ₄ ^g	NO	600 ppb	λ > 420 nm	–	50 mg	–	–	47 %/10 min	–	[166]
NCN/PI/RGO	NO	600 ppb	λ > 420 nm	–	20 mg	~120	–	60 %/10 min	–	[167]
CNK-OH&Fe ^h	IPA	1000 μmol	λ > 400 nm	8–9	50 mg	3.4 μmol (2 min)	In-situ	99 %/20 min TOC 99.9 %/ 36 h	–	[168]

^a CIP: ciprofloxacin hydrochloride.^b ENR: enrofloxacin.^c LOM: lomefloxacin.^d BNQDs/UPCN: boron nitride quantum dots/ultrathin porous g-C₃N₄.^e BPQDs: black phosphorus quantum dots.^f RFR: resorcinol-formaldehyde resins.^g PI: perylene imides.^h CNK-OH&Fe: Fe³⁺ modified K implanted and hydroxyl grafted C₃N₄.

Moon *et al.* [164] constructed a ternary photocatalytic system for the oxidation of arsenite. In this system, the modified carbon nitride reduced dissolved O₂ to produce H₂O₂ and WO₃ provided electrons to regenerated Fe²⁺ achieving the in-situ Fenton process. The As(III) can be oxidized to As(V) with lower toxicity and mobility, which can be easily removed via the adsorption process. However, organoarsenic compounds are more difficult to remove via conventional adsorption, precipitation, and coagulation methods than inorganic arsenic. Thus, it is necessary to oxidize organoarsenic compounds to inorganic arsenic before the adsorption. Li *et al.* [165] reported FeS₂ decorated

resorcinol-formaldehyde resin (FeS₂-RFR) photocatalyst, which can degrade roxarsone (ROX) into inorganic arsenic and then further oxidize into low toxic As(V). PFR and FeS₂ formed a type I heterojunction photocatalyst, in which the excited e⁻ migrated from PFR to FeS₂ for H₂O₂ production and promoted the circulation of Fe³⁺/Fe²⁺. The Fe²⁺ ionized from FeS₂ activates the H₂O₂ generated in situ to generate •OH. •OH broke the C-As bond on ROX, opened its ring to form maleic acid, and finally mineralized it to CO₂ and H₂O. The arsenious acid (As(III)) was selectively oxidized to arsenic acid (As(V)) by the •OH.

In addition to the removal of pollutants in the aqueous phase,

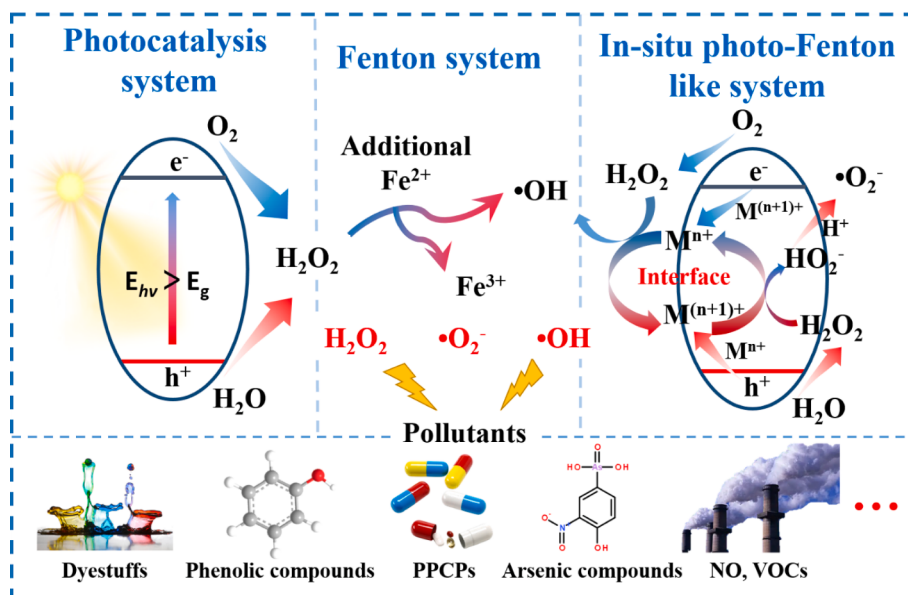


Fig. 10. Reaction mechanisms of pollutants degradation by different photocatalytic H_2O_2 production systems.

photocatalytic generation of H_2O_2 has also been attempted for the removal of pollutants in the gas phase. Nitric oxide (NO) is a common gaseous pollutant, which causes a series of environmental problems including acid rain, photochemical smog, and ozone depletion. Its concentration in the atmosphere has greatly increased with the increase of industrial activities and automobiles. In the photocatalysis system, the common processes are that NO is oxidized to NO_2 by the hole and O_2 is reduced to H_2O_2 by electron, then they react with each other to produce NO_3^- [166,167]. Generally, photocatalytic H_2O_2 production and in situ Fenton reaction rely on an acid aqueous-phase medium to provide sufficient H^+ and avoid the complexation of Fe^{3+} . Remarkably, Li *et al.* [168] loaded Fe^{3+} on alkalinized $\text{g-C}_3\text{N}_4$ to produce H_2O_2 and convert it to $\bullet\text{OH}$ through Fenton reaction for degradation of VOCs on a solid-gas interface. Unexpectedly, the alkaline surface of photocatalyst provided an appropriate environment for the Fenton process in the solid-gas interface attributing to the grafted hydroxyl groups. The hydroxyl groups grafted on the surface can be converted to $\bullet\text{OH}$ by the photohole channels, which can oxidize the IPA to provide H^+ for H_2O_2 production. Therefore, the degradation rate of IPA can reach 270 times that of pristine $\text{g-C}_3\text{N}_4$ through such a strategy of coupling the surface modification with the in-situ Fenton reaction. Besides, it also exhibited the efficient photocatalytic activities of other VOCs including aldehyde, ketone, carboxylic acid, and aromatic hydrocarbon, which proved that it is a universal and efficient strategy for the degradation of VOCs.

5. Conclusions and outlook

The solar-driven photocatalytic process provides an environmentally friendly and safe approach for H_2O_2 production, which shows great potential for in-situ environment applications. Up to now, many photocatalysts have been designed through various modification strategies. In this review, we have reviewed and discussed the effects and mechanisms of those design strategies based on three ways, i.e., light absorption, charge separation, and surface redox reaction. Then, we introduce the representative applications of photocatalytic H_2O_2 production in the environmental field.

Currently, the light utilization capacity of photocatalyst, the recombination of photogenerated electrons, the selectivity of H_2O_2 synthesis, and the in-situ decomposition of H_2O_2 are still the main factors that limit the production rate of H_2O_2 . Firstly, the AQY of photocatalysts is still low especially in the long-wavelength region. Although

the AQY of some photocatalysts was reported to reach 100 % in ultra-violet or short wave blue light region, it decreased rapidly with the increase of wavelength and approached zero above 500 nm. Therefore, new photocatalysts need to be designed to increase the light absorption capacity in visible light and enhance the SCC capacity.

Secondly, inhibiting the recombination and accelerating the migration of electrons are critical to improving photocatalytic production efficiency. In many studies, undesired sacrificial agents are used to consume the holes and provide electrons to avoid charge recombination, which brings extra cost and complexity to the reaction system. In this regard, constructing heterojunction or utilizing the different components with special properties to accelerate the separation of electron-hole pairs are more ideal.

Thirdly, the mechanism of surface redox reactions should be further explored to improve the selectivity of H_2O_2 production and inhibit the in-situ decomposition of H_2O_2 . The photocatalyst that can directly produce H_2O_2 through the 2e^- ORR or WOR pathway is preferred. The H_2O_2 decomposition can be minimized through surface hydrophobic modification or the construction of heterogeneous catalytic systems.

On the other hand, the mechanism of photocatalytic H_2O_2 production needs to be further explored. The transformation pathways between different ROS and their roles played in the whole process are not clear. Commonly used methods such as quenching experiments or ESR can only prove their existence and is difficult to confirm whether they participate in the reaction directly or act as an intermediate product of H_2O_2 . The different reaction paths and their impacts on ORR and WOR need to be investigated. Advanced in-situ characterization methods or theoretical simulations should be used to explore the mechanism, providing a theoretical basis for the design of photocatalyst and selective generation of H_2O_2 .

For the environmental applications of photocatalytic H_2O_2 generation, different performance enhancement strategies need to be selected based on the actual scenarios of environmental applications. It is necessary to consider the influence of complex matrices in water bodies such as inorganic ions and organics on H_2O_2 production. Considering the cost and potential harm to the environment, non-metal modification may be a better choice than noble metal modification for the catalyst. As for the disinfection that requires prolonged action and does not require high oxidative capacity, H_2O_2 can be directly produced for the inactivation of pathogens. For refractory pollutants, the in-situ Fenton reaction can be considered to increase the oxidation capacity. Obviously, it

has greater application potential in acidic or Fe-containing wastewater. The stability and recyclability of photocatalysts are also important in practical environment applications. The decomposition of organic components and the dissolution/consumption of ions of photocatalysts (especially in the Fenton system) need to be further optimized for the practical environment. Of course, developing recycling methods for photocatalysts and designing high-performance treatment devices are needed to ensure their technical and economic feasibility in environmental applications. We believe that more efficient photocatalysts for H₂O₂ production and more approaches for environmental applications would be developed if the above endeavours are achieved.

Declaration of Competing Interest

The authors declare that they have no known competing financial interests or personal relationships that could have appeared to influence the work reported in this paper.

Data availability

No data was used for the research described in the article.

Acknowledgements

This work was supported by the Fundamental Research Funds for the Central Universities (2022-4-ZD-08).

References:

- [1] J.M. Campos-Martin, G. Blanco-Brieva, J.L.G. Fierro, Hydrogen peroxide synthesis: An outlook beyond the Anthraquinone Process, *Angew. Chem. Int. Edit.* 45 (2006) 6962–6984, <https://doi.org/10.1002/anie.200503779>.
- [2] K. Kamata, K. Yonehara, Y. Sumida, K. Yamaguchi, S. Hikichi, N. Mizuno, Efficient epoxidation of olefins with ≥99% Selectivity and use of hydrogen peroxide, *Science* 300 (2003) 964–966, <https://doi.org/10.1126/science.1083176>.
- [3] K.P. Bryliakov, Catalytic asymmetric oxygenations with the environmentally benign oxidants H₂O₂ and O₂, *Chem. Rev.* 117 (2017) 11406–11459, <https://doi.org/10.1021/acscchemrev.7b00167>.
- [4] Z. Tang, P. Zhao, H. Wang, Y. Liu, W. Bu, Biomedicine meets fenton chemistry, *Chem. Rev.* 121 (2021) 1981–2019, <https://doi.org/10.1021/acs.chemrev.0c00977>.
- [5] X. Wang, X. Zhong, Z. Liu, L. Cheng, Recent progress of chemodynamic therapy-induced combination cancer therapy, *Nano Today* 35 (2020), 100946, <https://doi.org/10.1016/j.nantod.2020.100946>.
- [6] Y. Wang, Room-temperature conversion of methane becomes true, *Joule* 2 (2018) 1399–1401, <https://doi.org/10.1016/j.joule.2018.07.013>.
- [7] J. Tang, T. Zhao, D. Solanki, X. Miao, W. Zhou, S. Hu, Selective hydrogen peroxide conversion tailored by surface, interface, and device engineering, *Joule* 5 (2021) 1432–1461, <https://doi.org/10.1016/j.joule.2021.04.012>.
- [8] D.B. Miklos, C. Remy, M. Jekel, K.G. Linden, J.E. Drewes, U. Hübner, Evaluation of advanced oxidation processes for water and wastewater treatment - A critical review, *Water Res.* 139 (2018) 118–131, <https://doi.org/10.1016/j.watres.2018.03.042>.
- [9] J. Xu, X. Zheng, Z. Feng, Z. Lu, Z. Zhang, W. Huang, Y. Li, D. Vuckovic, Y. Li, S. Dai, G. Chen, K. Wang, H. Wang, J.K. Chen, W. Mitch, Y. Cui, Organic wastewater treatment by a single-atom catalyst and electrolytically produced H₂O₂, *Nat. Sustain.* 4 (2021) 233–241, <https://doi.org/10.1038/s41893-020-00635-w>.
- [10] L. Pi, J. Cai, L. Xiong, J. Cui, H. Hua, D. Tang, X. Mao, Generation of H₂O₂ by on-site activation of molecular dioxygen for environmental remediation applications: A review, *Chem. Eng. J.* 389 (2020), 123420, <https://doi.org/10.1016/j.cej.2019.123420>.
- [11] U. von Gunten, Oxidation Processes in Water Treatment: Are We on Track? *Environ. Sci. Technol.* 52 (2018) 5062–5075, <https://doi.org/10.1021/acs.est.8b00586>.
- [12] F. Ye, T. Wang, X. Quan, H. Yu, S. Chen, Constructing efficient WO₃-FPC system for photoelectrochemical H₂O₂ production and organic pollutants degradation, *Chem. Eng. J.* 389 (2020), 123427, <https://doi.org/10.1016/j.cej.2019.123427>.
- [13] H. Dai, H. He, C. Lai, Z. Xu, X. Zheng, G. Yu, B. Huang, X. Pan, D.D. Dionysiou, Modified humic acids mediate efficient mineralization in a photo-bio-electro-Fenton process, *Water Res.* 190 (2021), 116740, <https://doi.org/10.1016/j.watres.2020.116740>.
- [14] W. Wang, Q. Wu, N. Huang, Z. Xu, M. Lee, H. Hu, Potential risks from UV/H₂O₂ oxidation and UV photocatalysis: A review of toxic, assimilable, and sensory-unpleasant transformation products, *Water Res.* 141 (2018) 109–125, <https://doi.org/10.1016/j.watres.2018.05.005>.
- [15] T. Richards, J.H. Harrhy, R.J. Lewis, A.G.R. Howe, G.M. Suldecki, A. Folli, D. J. Morgan, T.E. Davies, E.J. Loveridge, D.A. Crole, J.K. Edwards, P. Gaskin, C. J. Kiely, Q. He, D.M. Murphy, J. Maillard, S.J. Freakley, G.J. Hutchings, A residue-free approach to water disinfection using catalytic in situ generation of reactive oxygen species, *Nat. Catal.* 4 (2021) 575–585, <https://doi.org/10.1038/s41929-021-00642-w>.
- [16] H. Hou, X. Zeng, X. Zhang, Production of hydrogen peroxide by photocatalytic processes, *Angew. Chem. Int. Edit.* 59 (2020) 17356–17376, <https://doi.org/10.1002/anie.201911609>.
- [17] S.J. Freakley, Q. He, J.H. Harrhy, L. Lu, D.A. Crole, D.J. Morgan, E.N. Ntaijinja, J. K. Edwards, A.F. Carley, A.Y. Borisevich, C.J. Kiely, G.J. Hutchings, Palladium-tin catalysts for the direct synthesis of H₂O₂ with high selectivity, *Science* 351 (2016) 965–968, <https://doi.org/10.1126/science.aad5705>.
- [18] S. Siahrostami, A. Verdaguer-Casadevall, M. Karamad, D. Deiana, P. Malacrida, B. Wickman, M. Escudero-Escribano, E.A. Paoli, R. Frydendal, T.W. Hansen, I. Chorkendorff, I.E.L. Stephens, J. Rossmeisl, Enabling direct H₂O₂ production through rational electrocatalyst design, *Nat. Mater.* 12 (2013) 1137–1143, <https://doi.org/10.1038/nmat3795>.
- [19] J.K. Edwards, B. Solsona, E.N. N, A.F. Carley, A.A. Herzing, C.J. Kiely, G. J. Hutchings, Switching off hydrogen peroxide hydrogenation in the direct synthesis process, *Science* 323 323 (5917) (2009) 1037–1041, <https://doi.org/10.1126/science.1168980>.
- [20] C. Xia, Y. Xia, P. Zhu, L. Fan, H. Wang, Direct electrosynthesis of pure aqueous H₂O₂ solutions up to 20% by weight using a solid electrolyte, *Science* 366 (2019) 226–231, <https://doi.org/10.1126/science.aay1844>.
- [21] C. Xia, S. Back, S. Ringe, K. Jiang, F. Chen, X. Sun, S. Siahrostami, K. Chan, H. Wang, Confined local oxygen gas promotes electrochemical water oxidation to hydrogen peroxide, *Nat. Catal.* 3 (2020) 125–134, <https://doi.org/10.1038/s41929-019-0402-8>.
- [22] Y. Nosaka, A.Y. Nosaka, Generation and detection of reactive oxygen species in photocatalysis, *Chem. Rev.* 117 (2017) 11302–11336, <https://doi.org/10.1021/acscchemrev.7b00161>.
- [23] S. Giannakis, M. Voumard, S. Rtimi, C. Pulgarin, Bacterial disinfection by the photo-Fenton process: Extracellular oxidation or intracellular photo-catalysis? *Appl. Catal. B: Environ.* 227 (2018) 285–295, <https://doi.org/10.1016/j.apcatb.2018.01.044>.
- [24] J. Lin, W. Tian, Z. Guan, H. Zhang, X. Duan, H. Wang, H. Sun, Y. Fang, Y. Huang, S. Wang, Functional carbon nitride materials in photo-fenton-like catalysis for environmental remediation, *Adv. Funct. Mater.* 32 (2022) 2201743, <https://doi.org/10.1002/adfm.202201743>.
- [25] Y. Zhu, R. Zhu, Y. Xi, J. Zhu, G. Zhu, H. He, Strategies for enhancing the heterogeneous Fenton catalytic reactivity: A review, *Appl. Catal. B: Environ.* 255 (2019), 117739, <https://doi.org/10.1016/j.apcatb.2019.05.041>.
- [26] Q. Guo, C. Zhou, Z. Ma, Z. Ren, H. Fan, X. Yang, Elementary photocatalytic chemistry on TiO₂ surfaces, *Chem. Soc. Rev.* 45 (2016) 3701–3730, <https://doi.org/10.1039/C5CS00448A>.
- [27] J. Lim, H. Kim, J. Park, G. Moon, J.J.M. Vequizo, A. Yamakata, J. Lee, W. Choi, How g-C₃N₄ works and is different from TiO₂ as an environmental photocatalyst: mechanistic view, *Environ. Sci. Technol.* 54 (2020) 497–506, <https://doi.org/10.1016/j.est.2019.05.044>.
- [28] A. Torres-Pinto, M.J. Sampaio, C.G. Silva, J.L. Faria, A.M.T. Silva, Recent strategies for hydrogen peroxide production by metal-free carbon nitride photocatalysts, *Catalysts* 9 (2019) 990, <https://doi.org/10.3390/catal9120990>.
- [29] B. Yan, Z. Chen, Y. Xu, Amorphous and crystalline 2D polymeric carbon nitride nanosheets for photocatalytic hydrogen/oxygen evolution and hydrogen peroxide production, *Chem.-Asian J.* 15 (2020) 2329–2340, <https://doi.org/10.1002/asia.202000253>.
- [30] Z. Haider, H. Cho, G. Moon, H. Kim, Minireview: Selective production of hydrogen peroxide as a clean oxidant over structurally tailored carbon nitride photocatalysts, *Catal. Today* 335 (2019) 55–64, <https://doi.org/10.1016/j.cattod.2018.11.067>.
- [31] H. Tada, Overall water splitting and hydrogen peroxide synthesis by gold nanoparticle-based plasmonic photocatalysts, *Nanoscale Adv.* 1 (2019) 4238–4245, <https://doi.org/10.1039/C9NA00431A>.
- [32] X. Hu, X. Zeng, Y. Liu, J. Lu, X. Zhang, Carbon-based materials for photo- and electrocatalytic synthesis of hydrogen peroxide, *Nanoscale* 12 (2020) 16008–16027, <https://doi.org/10.1039/DONR03178J>.
- [33] L. Wang, J. Zhang, Y. Zhang, H. Yu, Y. Qu, J. Yu, Inorganic metal-oxide photocatalyst for H₂O₂ Production, *Small* 18 (2022) 2104561, <https://doi.org/10.1002/smll.202104561>.
- [34] X. Zeng, Y. Liu, X. Hu, X. Zhang, Photoredox catalysis over semiconductors for light-driven hydrogen peroxide production, *Green Chem.* 23 (2021) 1466–1494, <https://doi.org/10.1039/D0GC04236F>.
- [35] Y. Sun, L. Han, P. Strasser, A comparative perspective of electrochemical and photochemical approaches for catalytic H₂O₂ production, *Chem. Soc. Rev.* 49 (2020) 6605–6631, <https://doi.org/10.1039/D0CS00458H>.
- [36] Y. Zhao, P. Zhang, Z. Yang, L. Li, J. Gao, S. Chen, T. Xie, C. Diao, S. Xi, B. Xiao, C. Hu, W. Choi, Mechanistic analysis of multiple processes controlling solar-driven H₂O₂ synthesis using engineered polymeric carbon nitride, *Nat. Commun.* 12 (2021) 3701, <https://doi.org/10.1038/s41467-021-24048-1>.
- [37] Q. Guo, C. Zhou, Z. Ma, X. Yang, Fundamentals of TiO₂ Photocatalysis: Concepts, Mechanisms, and Challenges, *Adv. Mater.* 31 (2019) 1901997, <https://doi.org/10.1002/adma.201901997>.
- [38] J. Schneider, M. Matsuoka, M. Takeuchi, J. Zhang, Y. Horiuchi, M. Anpo, D. W. Bahnemann, Understanding TiO₂ photocatalysis: mechanisms and materials, *Chem. Rev.* 114 (2014) 9919–9986, <https://doi.org/10.1021/cr5001892>.

- [39] L. Wang, Q. Zhang, B. Chen, Y. Bu, Y. Chen, J. Ma, F.L. Rosario-Ortiz, R. Zhu, Some issues limiting photo(catalysis) application in water pollutant control: A critical review from chemistry perspectives, *Water Res.* 174 (2020), 115605, <https://doi.org/10.1016/j.watres.2020.115605>.
- [40] Z. Teng, W. Cai, S. Liu, C. Wang, Q. Zhang, S. Chenliang, T. Ohno, Bandgap engineering of polymeric carbon nitride copolymerized by 2,5,8-triamino-tri-s-triazine (melem) and barbituric acid for efficient nonsacrificial photocatalytic H₂O₂ production, *Appl. Catal. B: Environ.* 271 (2020), 118917, <https://doi.org/10.1016/j.apcatb.2020.118917>.
- [41] P. Zhang, D. Sun, A. Cho, S. Weon, S. Lee, J. Lee, J.W. Han, D. Kim, W. Choi, Modified carbon nitride nanzyme as bifunctional glucose oxidase-peroxidase for metal-free bioinspired cascade photocatalysis, *Nat. Commun.* 10 (2019) 940, <https://doi.org/10.1038/s41467-019-08731-y>.
- [42] P. Zhang, Y. Tong, Y. Liu, J.J.M. Vequizo, H. Sun, C. Yang, A. Yamakata, F. Fan, W. Lin, X. Wang, W. Choi, Heteroatom dopants promote two-electron O₂ reduction for photocatalytic production of H₂O₂ on polymeric carbon Nitride, *Angew. Chem. Int. Edit.* 59 (2020) 16209–16217, <https://doi.org/10.1002/anie.202006747>.
- [43] Y. Hou, F. Zuo, A. Dagg, P. Feng, A three-dimensional branched cobalt-doped α -Fe₂O₃ Nanorod/MgFe₂O₄ heterojunction array as a flexible photoanode for efficient photoelectrochemical water oxidation, *Angew. Chem. Int. Edit.* 52 (2013) 1248–1252, <https://doi.org/10.1002/anie.201207578>.
- [44] S. Li, G. Dong, R. Haili, L. Yang, Y. Li, F. Wang, Y. Zeng, C. Wang, Effective photocatalytic H₂O₂ production under visible light irradiation at g-C₃N₄ modulated by carbon vacancies, *Appl. Catal. B: Environ.* 190 (2016) 26–35, <https://doi.org/10.1016/j.apcatb.2016.03.004>.
- [45] Z. Zhu, H. Pan, M. Muruganathan, J. Gong, Y. Zhang, Visible light-driven photocatalytically active g-C₃N₄ material for enhanced generation of H₂O₂, *Appl. Catal. B: Environ.* 232 (2018) 19–25, <https://doi.org/10.1016/j.apcatb.2018.03.035>.
- [46] L. Shi, L. Yang, W. Zhou, Y. Liu, L. Yin, X. Hai, H. Song, J. Ye, Photoassisted construction of holey defective g-C₃N₄ photocatalysts for efficient visible-light-driven H₂O₂ Production, *Small* 14 (2018) 1703142, <https://doi.org/10.1002/smll.201703142>.
- [47] Y. Xie, Y. Li, Z. Huang, J. Zhang, X. Jia, X. Wang, J. Ye, Two types of cooperative nitrogen vacancies in polymeric carbon nitride for efficient solar-driven H₂O₂ evolution, *Appl. Catal. B: Environ.* 265 (2020), 118581, <https://doi.org/10.1016/j.apcatb.2019.118581>.
- [48] H. Kim, O.S. Kwon, S. Kim, W. Choi, J. Kim, Harnessing low energy photons (635 nm) for the production of H₂O₂ using upconversion nanohybrid photocatalysts, *Energ. Environ. Sci.* 9 (2016) 1063–1073, <https://doi.org/10.1039/C5EE03115J>.
- [49] X. Chen, W. Zhang, L. Zhang, L. Feng, C. Zhang, J. Jiang, T. Yan, H. Wang, Sacrificial agent-free photocatalytic H₂O₂ evolution via two-electron oxygen reduction using a ternary α -Fe₂O₃/CQD@g-C₃N₄ photocatalyst with broad-spectrum response, *J. Mater. Chem. A* 8 (2020) 18816–18825, <https://doi.org/10.1039/DOTA05753C>.
- [50] Y. Liu, Y. Zhao, Y. Sun, J. Cao, H. Wang, X. Wang, H. Huang, M. Shao, Y. Liu, Z. Kang, A 4e-2e- cascaded pathway for highly efficient production of H₂ and H₂O₂ from water photo-splitting at normal pressure, *Appl. Catal. B: Environ.* 270 (2020), 118875, <https://doi.org/10.1016/j.apcatb.2020.118875>.
- [51] Y. Li, Y. Zhao, H. Nie, K. Wei, J. Cao, H. Huang, M. Shao, Y. Liu, Z. Kang, Interface photo-charge kinetics regulation by carbon dots for efficient hydrogen peroxide production, *J. Mater. Chem. A* 9 (2021) 515–522, <https://doi.org/10.1039/DOTA10231H>.
- [52] C. Xia, H. Wang, J.K. Kim, J. Wang, Rational design of metal oxide-based heterostructure for efficient photocatalytic and photoelectrochemical systems, *Adv. Funct. Mater.* 31 (2021) 2008247, <https://doi.org/10.1002/adfm.202008247>.
- [53] M. Teranishi, R. Hoshino, S. Naya, H. Tada, Gold-nanoparticle-loaded carbonate-modified titanium(iv) oxide surface: visible-light-driven formation of hydrogen peroxide from oxygen, *Angew. Chem. Int. Edit.* 55 (2016) 12773–12777, <https://doi.org/10.1002/anie.201606734>.
- [54] J. Cai, J. Huang, S. Wang, J. Iocozzia, Z. Sun, J. Sun, Y. Yang, Y. Lai, Z. Lin, Crafting mussel-inspired metal nanoparticle-decorated ultrathin graphitic carbon nitride for the degradation of chemical pollutants and production of chemical resources, *Adv. Mater.* 31 (2019) 1806314, <https://doi.org/10.1002/adma.201806314>.
- [55] H. Shi, Y. Li, X. Wang, H. Yu, J. Yu, Selective modification of ultra-thin g-C₃N₄ nanosheets on the (110) facet of Au/BiVO₄ for boosting photocatalytic H₂O₂ production, *Appl. Catal. B: Environ.* 297 (2021), 120414, <https://doi.org/10.1016/j.apcatb.2021.120414>.
- [56] X. Yu, C. Hu, D. Hao, G. Liu, R. Xu, X. Zhu, X. Yu, Y. Ma, L. Ma, Tubular carbon nitride with hierarchical network: localized charge carrier generation and reduced charge recombination for high-performance photocatalysis of H₂ and H₂O₂ Production, *Solar RRL* (2021) 2000827, <https://doi.org/10.1002/solr.202000827>.
- [57] X. Chen, W. Zhang, L. Zhang, L. Feng, C. Zhang, J. Jiang, H. Wang, Construction of porous tubular In₂S₃@In₂O₃ with plasma treatment-derived oxygen vacancies for efficient photocatalytic h₂O₂ production in pure water via two-electron reduction, *ACS Appl. Mater. Inter.* 13 (2021) 25868–25878, <https://doi.org/10.1021/acsami.1c02953>.
- [58] Q. Wu, Y. Liu, J. Cao, Y. Sun, F. Liao, Y. Liu, H. Huang, M. Shao, Z. Kang, A function-switchable metal-free photocatalyst for the efficient and selective production of hydrogen and hydrogen peroxide, *J. Mater. Chem. A* 8 (2020) 11773–11780, <https://doi.org/10.1039/DOTA03974H>.
- [59] Y. Shiraishi, T. Takii, T. Hagi, S. Mori, Y. Kofuji, Y. Kitagawa, S. Tanaka, S. Ichikawa, T. Hirai, Resorcinol-formaldehyde resins as metal-free semiconductor photocatalysts for solar-to-hydrogen peroxide energy conversion, *Nat. Mater.* 18 (2019) 985–993, <https://doi.org/10.1038/s41563-019-0398-0>.
- [60] L. Liu, M. Gao, H. Yang, X. Wang, X. Li, A.I. Cooper, Linear conjugated polymers for solar-driven hydrogen peroxide production: the importance of catalyst stability, *J. Am. Chem. Soc.* 143 (2021) 19287–19293, <https://doi.org/10.1021/jacs.1c00979>.
- [61] Z. Tian, C. Han, Y. Zhao, W. Dai, X. Lian, Y. Wang, Y. Zheng, Y. Shi, X. Pan, Z. Huang, H. Li, W. Chen, Efficient photocatalytic hydrogen peroxide generation coupled with selective benzylamine oxidation over defective ZrS₃ nanobelts, *Nat. Commun.* 12 (2021) 2039, <https://doi.org/10.1038/s41467-021-22394-8>.
- [62] Q. Wu, J. Cao, X. Wang, Y. Liu, Y. Zhao, H. Wang, Y. Liu, H. Huang, F. Liao, M. Shao, Z. Kang, A metal-free photocatalyst for highly efficient hydrogen peroxide photoproduction in real seawater, *Nat. Commun.* 12 (2021) 483, <https://doi.org/10.1038/s41467-020-20823-8>.
- [63] M. Liu, Y. Pang, B. Zhang, P. De Luna, O. Voznyj, J. Xu, X. Zheng, C.T. Dinh, F. Fan, C. Cao, F.P.G. de Arquer, T.S. Safaei, A. Mepham, A. Klinkova, E. Kumacheva, T. Filletter, D. Sinton, S.O. Kelley, E.H. Sargent, Enhanced electrocatalytic CO₂ reduction via field-induced reagent concentration, *Nature* 537 (2016) 382–386, <https://doi.org/10.1038/nature19060>.
- [64] Z. Zeng, X. Quan, H. Yu, S. Chen, S. Zhang, Nanoscale lightning rod effect in 3D carbon nitride nanoneedle: Enhanced charge collection and separation for efficient photocatalysis, *J. Catal.* 375 (2019) 361–370, <https://doi.org/10.1016/j.jcat.2019.06.019>.
- [65] C. Feng, L. Tang, Y. Deng, J. Wang, Y. Liu, X. Ouyang, H. Yang, J. Yu, J. Wang, A novel sulfur-assisted annealing method of g-C₃N₄ nanosheet compensates for the loss of light absorption with further promoted charge transfer for photocatalytic production of H₂ and H₂O₂, *Appl. Catal. B: Environ.* 281 (2021), 119539, <https://doi.org/10.1016/j.apcatb.2020.119539>.
- [66] L. Zhou, J. Feng, B. Qiu, Y. Zhou, J. Lei, M. Xing, L. Wang, Y. Zhou, Y. Liu, J. Zhang, Ultrathin g-C₃N₄ nanosheet with hierarchical pores and desirable energy band for highly efficient H₂O₂ production, *Appl. Catal. B: Environ.* 267 (2020), 118396, <https://doi.org/10.1016/j.apcatb.2019.118396>.
- [67] X. Zhang, P. Ma, C. Wang, L. Gan, X. Chen, P. Zhang, Y. Wang, H. Li, L. Wang, X. Zhou, K. Zheng, Unraveling the dual defect sites in graphite carbon nitride for ultra-high photocatalytic H₂O₂ evolution, *Energ. Environ. Sci.* 15 (2022) 830–842, <https://doi.org/10.1039/DIEE02369A>.
- [68] J. Barber, Photosynthetic energy conversion: natural and artificial, *Chem. Soc. Rev.* 38 (2009) 185–196, <https://doi.org/10.1039/B802262N>.
- [69] Y. Yang, C. Zhang, D. Huang, G. Zeng, J. Huang, C. Lai, C. Zhou, W. Wang, H. Guo, W. Xue, R. Deng, M. Cheng, W. Xiong, Boron nitride quantum dots decorated ultrathin porous g-C₃N₄: Intensified exciton dissociation and charge transfer for promoting visible-light-driven molecular oxygen activation, *Appl. Catal. B: Environ.* 245 (2019) 87–99, <https://doi.org/10.1016/j.apcatb.2018.12.049>.
- [70] L. Zheng, H. Su, J. Zhang, L.S. Walekar, H. Vafaei Molamahmood, B. Zhou, M. Long, Y.H. Hu, Highly selective photocatalytic production of H₂O₂ on sulfur and nitrogen co-doped graphene quantum dots tuned TiO₂, *Appl. Catal. B: Environ.* 239 (2018) 475–484, <https://doi.org/10.1016/j.apcatb.2018.08.031>.
- [71] R. Ma, L. Wang, H. Wang, Z. Liu, M. Xing, L. Zhu, X. Meng, F. Xiao, Solid acids accelerate the photocatalytic hydrogen peroxide synthesis over a hybrid catalyst of titania nanotube with carbon dot, *Appl. Catal. B: Environ.* 244 (2019) 594–603, <https://doi.org/10.1016/j.apcatb.2018.11.087>.
- [72] Y. Liu, Y. Zhao, Q. Wu, X. Wang, H. Nie, Y. Zhou, H. Huang, M. Shao, Y. Liu, Z. Kang, Charge storage of carbon dot enhances photo-production of H₂ and H₂O₂ over Ni₂P/carbon dot catalyst under normal pressure, *Chem. Eng. J.* 409 (2021), 128184, <https://doi.org/10.1016/j.cej.2020.128184>.
- [73] C. Chu, W. Miao, Q. Li, D. Wang, Y. Liu, S. Mao, Highly efficient photocatalytic H₂O₂ production with cyano and SnO₂ co-modified g-C₃N₄, *Chem. Eng. J.* 428 (2022), 132531, <https://doi.org/10.1016/j.cej.2021.132531>.
- [74] S. Jiang, C. Xiong, S. Song, B. Cheng, Plasmonic Graphene-Like Au/C₃N₄ nanosheets with barrier-free interface for photocatalytically sustainable evolution of active oxygen species, *ACS Sustain. Chem. Eng.* 7 (2019) 2018–2026, <https://doi.org/10.1021/acssuschemeng.8b04338>.
- [75] K. Kim, J. Park, H. Kim, G.Y. Jung, M. Kim, Solid-phase photocatalysts: physical vapor deposition of Au nanoislands on porous TiO₂ films for millimolar H₂O₂ production within few minutes, *ACS Catal.* 9 (2019) 9206–9211, <https://doi.org/10.1021/acscatal.9b02269>.
- [76] C. Liu, T. Bao, L. Yuan, C. Zhang, J. Wang, J. Wan, C. Yu, Semiconducting MOF@ZnS heterostructures for photocatalytic hydrogen peroxide production: heterojunction coverage matters, *Adv. Funct. Mater.* 32 (15) (2022) 2111404, <https://doi.org/10.1002/adfm.202111404>.
- [77] Y. Ye, J. Pan, F. Xie, L. Gong, S. Huang, Z. Ke, F. Zhu, J. Xu, and G. Ouyang, Highly efficient photosynthesis of hydrogen peroxide in ambient conditions. *Proc. Natl. Acad. Sci. U. S. A.* 118 (2021) e2103964118, <http://doi.org/10.1073/pnas.2103964118>.
- [78] H. Che, X. Gao, J. Chen, J. Hou, Y. Ao, P. Wang, Iodide-induced fragmentation of polymerized hydrophilic carbon nitride for high-performance quasi-homogeneous photocatalytic H₂O₂ Production, *Angew. Chem. Int. Edit.* 60 (2021) 25546–25550, <https://doi.org/10.1002/anie.202111769>.
- [79] X. Dang, R. Yang, Z. Wang, S. Wu, H. Zhao, Efficient visible-light activation of molecular oxygen to produce hydrogen peroxide using P doped g-C₃N₄ hollow spheres, *J. Mater. Chem. A* 8 (2020) 22720–22727, <https://doi.org/10.1039/DOTA07794A>.

- [80] D. Wang, D. Su, Heterogeneous nanocarbon materials for oxygen reduction reaction, *Energ. Environ. Sci.* 7 (2014) 576–591, <https://doi.org/10.1039/c3ee43463j>.
- [81] W. Miao, Y. Wang, Y. Liu, H. Qin, C. Chu, S. Mao, Persulfate-induced three coordinate nitrogen (N_3^-) vacancies in defective carbon nitride for enhanced photocatalytic H_2O_2 evolution, *Engineering* (2022), <https://doi.org/10.1016/j.eng.2021.12.016>.
- [82] C. Chu, D. Huang, Q. Zhu, E. Stavitski, J.A. Spies, Z. Pan, J. Mao, H.L. Xin, C. A. Schmuttenmaer, S. Hu, J. Kim, Electronic tuning of metal nanoparticles for highly efficient photocatalytic hydrogen peroxide production, *ACS Catal.* 9 (2019) 626–631, <https://doi.org/10.1021/acscatal.8b03738>.
- [83] Z. Liu, X. Sheng, D. Wang, X. Feng, Efficient hydrogen peroxide generation utilizing photocatalytic oxygen reduction at a triphase interface, *iScience* 17 (2019) 67–73, <https://doi.org/10.1016/j.isci.2019.06.023>.
- [84] L. Li, L. Xu, Z. Hu, J.C. Yu, Enhanced mass transfer of oxygen through a gas-liquid-solid interface for photocatalytic hydrogen peroxide production, *Adv. Funct. Mater.* 31 (52) (2021) 2106120, <https://doi.org/10.1002/adfm.202106120>.
- [85] L. Chen, S. Li, Z. Yang, C. Chen, C. Chu, B. Chen, Enhanced photocatalytic hydrogen peroxide production at a solid-liquid-air interface via microenvironment engineering, *Appl. Catal. B: Environ.* 305 (2022), 121066, <https://doi.org/10.1016/j.apcatb.2022.121066>.
- [86] H. Zhu, Q. Xue, G. Zhu, Y. Liu, X. Dou, X. Yuan, Decorating Pt@cyclodextrin nanoclusters on $C_{3}N_4/MXene$ for boosting the photocatalytic H_2O_2 production, *J. Mater. Chem. A* 9 (2021) 6872–6880, <https://doi.org/10.1039/D0TA10742E>.
- [87] Z. Kang, S. Lee, Carbon dots: advances in nanocarbon applications, *Nanoscale* 11 (2019) 19214–19224, <https://doi.org/10.1039/c9nr05647e>.
- [88] L. Zhou, J. Lei, F. Wang, L. Wang, M.R. Hoffmann, Y. Liu, S. In, J. Zhang, Carbon nitride nanotubes with in situ grafted hydroxyl groups for highly efficient spontaneous H_2O_2 production, *Appl. Catal. B: Environ.* 288 (2021), 119993, <https://doi.org/10.1016/j.apcatb.2021.119993>.
- [89] A. Fujishima, X. Zhang, D.A. Tryk, TiO_2 photocatalysis and related surface phenomena, *Surf. Sci. Rep.* 63 (2008) 515–582, <https://doi.org/10.1016/j.surfrep.2008.10.001>.
- [90] W. Ong, L. Tan, Y.H. Ng, S. Yong, S. Chai, Graphitic carbon nitride ($g-C_3N_4$)-based photocatalysts for artificial photosynthesis and environmental remediation: are we a step closer to achieving sustainability? *Chem. Rev.* 116 (2016) 7159–7329, <https://doi.org/10.1021/acs.chemrev.6b00075>.
- [91] Y. Shiraishi, S. Kanazawa, Y. Sugano, D. Tsukamoto, H. Sakamoto, S. Ichikawa, T. Hirai, Highly selective production of hydrogen peroxide on graphitic carbon nitride ($g-C_3N_4$) photocatalyst activated by visible light, *ACS Catal.* 4 (2014) 774–780, <https://doi.org/10.1021/cs401208c>.
- [92] Y. Shiraishi, S. Kanazawa, Y. Kofuji, H. Sakamoto, S. Ichikawa, S. Tanaka, T. Hirai, Sunlight-driven hydrogen peroxide production from water and molecular oxygen by metal-free photocatalysts, *Angew. Chem. Int. Edit.* 53 (2014) 13454–13459, <https://doi.org/10.1002/anie.201407938>.
- [93] J. Luo, Y. Liu, C. Fan, L. Tang, S. Yang, M. Liu, M. Wang, C. Feng, X. Ouyang, L. Wang, L. Xu, J. Wang, M. Yan, Direct attack and indirect transfer mechanisms dominated by reactive oxygen species for photocatalytic H_2O_2 production on $g-C_3N_4$ Possessing nitrogen vacancies, *ACS Catal.* 11 (2021) 11440–11450, <https://doi.org/10.1021/acscatal.1c03103>.
- [94] J. Luo, C. Fan, L. Tang, Y. Liu, Z. Gong, T. Wu, X. Zhen, C. Feng, H. Feng, L. Wang, L. Xu, M. Yan, Reveal Bronsted-Evans-Polanyi relation and attack mechanisms of reactive oxygen species for photocatalytic H_2O_2 production, *Appl. Catal. B: Environ.* 301 (2022), 120757, <https://doi.org/10.1016/j.apcatb.2021.120757>.
- [95] Y. Shiraishi, S. Kanazawa, D. Tsukamoto, A. Shiro, Y. Sugano, T. Hirai, Selective hydrogen peroxide formation by titanium dioxide photocatalysis with benzylic alcohols and molecular oxygen in water, *ACS Catal.* 3 (2013) 2222–2227, <https://doi.org/10.1021/cs400511q>.
- [96] Y. Kofuji, Y. Isobe, Y. Shiraishi, H. Sakamoto, S. Tanaka, S. Ichikawa, T. Hirai, Carbon nitride-aromatic diimide-graphene nanohybrids: metal-free photocatalysts for solar-to-hydrogen peroxide energy conversion with 0.2% Efficiency, *J. Am. Chem. Soc.* 138 (2016) 10019–10025, <https://doi.org/10.1021/jacs.6b05806>.
- [97] J. Zhang, L. Zheng, F. Wang, C. Chen, H. Wu, S.A.K. Leghari, M. Long, The critical role of furfural alcohol in photocatalytic H_2O_2 production on TiO_2 , *Appl. Catal. B: Environ.* 269 (2020), 118770, <https://doi.org/10.1016/j.apcatb.2020.118770>.
- [98] Z. Teng, Q. Zhang, H. Yang, K. Kato, W. Yang, Y. Lu, S. Liu, C. Wang, A. Yamakata, C. Su, B. Liu, T. Ohno, Atomically dispersed antimony on carbon nitride for the artificial photosynthesis of hydrogen peroxide, *Nat. Catal.* 4 (2021) 374–384, <https://doi.org/10.1038/s41929-021-00605-1>.
- [99] Z. Teng, W. Cai, W. Sim, Q. Zhang, C. Wang, C. Su, T. Ohno, Photoexcited single metal atom catalysts for heterogeneous photocatalytic H_2O_2 production: Pragmatic guidelines for predicting charge separation, *Appl. Catal. B: Environ.* 282 (2021), 119589, <https://doi.org/10.1016/j.apcatb.2020.119589>.
- [100] S. Cao, T. Chan, Y. Lu, X. Shi, B. Fu, Z. Wu, H. Li, K. Liu, S. Alzuabi, P. Cheng, M. Liu, T. Li, X. Chen, L. Piao, Photocatalytic pure water splitting with high efficiency and value by Pt/porous brookite TiO_2 nanoflutes, *Nano Energy* 67 (2020), 104287, <https://doi.org/10.1016/j.nanoen.2019.104287>.
- [101] M. Zhu, C. Zhu, D. Wu, X. Wang, H. Wang, J. Gao, H. Huang, C. Shi, Y. Liu, Z. Kang, Efficient photocatalytic water splitting through titanium silicalite stabilized CoO nanodots, *Nanoscale* 11 (2019) 15984–15990, <https://doi.org/10.1039/C9NR05057D>.
- [102] D. Wei, Y. Tan, Y. Wang, T. Kong, S. Shen, S.S. Mao, Function-switchable metal-semiconductor junction enables efficient photocatalytic overall water splitting with selective water oxidation products, *Sci. Bull.* 65 (2020) 1389–1395, <https://doi.org/10.1016/j.scib.2020.04.042>.
- [103] X. Li, B. Kang, F. Dong, Z. Zhang, X. Luo, L. Han, J. Huang, Z. Feng, Z. Chen, J. Xu, B. Peng, Z.L. Wang, Enhanced photocatalytic degradation and H_2/H_2O_2 production performance of S-pCN/ $WO_{2.72}$ -S-scheme heterojunction with appropriate surface oxygen vacancies, *Nano Energy* 81 (2021), 105671, <https://doi.org/10.1016/j.nanoen.2020.105671>.
- [104] Y. Kofuji, S. Ohkita, Y. Shiraishi, H. Sakamoto, S. Tanaka, S. Ichikawa, T. Hirai, Graphitic carbon nitride doped with biphenyl diimide: efficient photocatalyst for hydrogen peroxide production from water and molecular oxygen by sunlight, *ACS Catal.* 6 (2016) 7021–7029, <https://doi.org/10.1021/acscatal.6b02367>.
- [105] Y. Kofuji, S. Ohkita, Y. Shiraishi, H. Sakamoto, S. Ichikawa, S. Tanaka, T. Hirai, Mellitic triimide-doped carbon nitride as sunlight-driven photocatalysts for hydrogen peroxide production, *ACS Sustain. Chem. Eng.* 5 (2017) 6478–6485, <https://doi.org/10.1021/acssuschemeng.7b00575>.
- [106] C. Chu, Q. Zhu, Z. Pan, S. Gupta, D. Huang, Y. Du, S. Weon, Y. Wu, C. Muhich, E. Stavitski, K. Domen, J. Kim, Spatially separating redox centers on 2D carbon nitride with cobalt single atom for photocatalytic H_2O_2 production, *Proc. Natl. Acad. Sci. U. S. A.* 117 (2020) 6376–6382, <https://doi.org/10.1073/pnas.1913403117>.
- [107] T. Liu, Z. Pan, J.M. Vequizo, K. Kato, B. Wu, A. Yamakata, K. Katayama, B. Chen, C. Chu, K. Domen, Overall photosynthesis of H_2O_2 by an inorganic semiconductor, *Nat. Commun.* 13 (2022) 1034, <https://doi.org/10.1038/s41467-022-28686-x>.
- [108] L. Chen, L. Wang, Y. Wan, Y. Zhang, Z. Qi, X. Wu, H. Xu, Acetylene and diacetylene functionalized covalent triazine frameworks as metal-free photocatalysts for hydrogen peroxide production: a new two-electron water oxidation pathway, *Adv. Mater.* 32 (2020) 1904433, <https://doi.org/10.1002/adma.201904433>.
- [109] C. Chu, Q. Li, W. Miao, Y. Qin, X. Liu, D. Yao, S. Mao, Photocatalytic H_2O_2 production driven by cyclodextrin-pyrimidine polymer in a wide pH range without electron donor or oxygen aeration, *Appl. Catal. B: Environ.* 314 (2022), 121485, <https://doi.org/10.1016/j.apcatb.2022.121485>.
- [110] Y. Zhao, Y. Liu, J. Cao, H. Wang, M. Shao, H. Huang, Y. Liu, Z. Kang, Efficient production of H_2O_2 via two-channel pathway over ZIF-8/ C_3N_4 composite photocatalyst without any sacrificial agent, *Appl. Catal. B: Environ.* 278 (2020), 119289, <https://doi.org/10.1016/j.apcatb.2020.119289>.
- [111] Y. Zhao, Y. Liu, Z. Wang, Y. Ma, Y. Zhou, X. Shi, Q. Wu, X. Wang, M. Shao, H. Huang, Y. Liu, Z. Kang, Carbon nitride assisted 2D conductive metal-organic frameworks composite photocatalyst for efficient visible light-driven H_2O_2 production, *Appl. Catal. B: Environ.* 289 (2021), 120035, <https://doi.org/10.1016/j.apcatb.2021.120035>.
- [112] X. Zhao, Y. You, S. Huang, Y. Wu, Y. Ma, G. Zhang, Z. Zhang, Z-scheme photocatalytic production of hydrogen peroxide over Bi_4O_5Br 2/ $g-C_3N_4$ heterostructure under visible light, *Appl. Catal. B: Environ.* 278 (2020), 119251, <https://doi.org/10.1016/j.apcatb.2020.119251>.
- [113] J. Wang, L. Yang, L. Zhang, Constructed 3D hierarchical micro-flowers $CoWO_4$ @ Bi_2WO_6 Z-scheme heterojunction catalyst: Two-channel photocatalytic H_2O_2 production and antibiotics degradation, *Chem. Eng. J.* 420 (2021), 127639, <https://doi.org/10.1016/j.cej.2020.127639>.
- [114] Z. He, C. Kim, L. Lin, T.H. Jeon, S. Lin, X. Wang, W. Choi, Formation of heterostructures via direct growth CN on h-BN porous nanosheets for metal-free photocatalysis, *Nano Energy* 42 (2017) 58–68, <https://doi.org/10.1016/j.nanoen.2017.10.043>.
- [115] J. Zhang, C. Yu, J. Lang, Y. Zhou, B. Zhou, Y.H. Hu, M. Long, Modulation of Lewis acidic-basic sites for efficient photocatalytic H_2O_2 production over potassium intercalated tri-s-triazine materials, *Appl. Catal. B: Environ.* 277 (2020), 119225, <https://doi.org/10.1016/j.apcatb.2020.119225>.
- [116] C. Krishnaraj, H. Sekhar Jena, L. Bourda, A. Laemont, P. Pachfule, J. Roeser, C. V. Chandran, S. Borgmans, S.M.J. Rogge, K. Leus, C.V. Stevens, J.A. Martens, V. Van Speybroeck, E. Breyneart, A. Thomas, P., Van der voort, strongly reducing (diarylaminobenzene-based covalent organic framework for metal-free visible light photocatalytic H_2O_2 Generation, *J. Am. Chem. Soc.* 142 (2020) 20107–20116, <https://doi.org/10.1021/jacs.0c09684>.
- [117] Y. Yang, G. Zeng, D. Huang, C. Zhang, D. He, C. Zhou, W. Wang, W. Xiong, X. Li, B. Li, W. Dong, Y. Zhou, Molecular engineering of polymeric carbon nitride for highly efficient photocatalytic oxytetracycline degradation and H_2O_2 production, *Appl. Catal. B: Environ.* 272 (2020), 118970, <https://doi.org/10.1016/j.apcatb.2020.118970>.
- [118] Y. Dong, Q. Han, Q. Hu, C. Xu, C. Dong, Y. Peng, Y. Ding, Y. Lan, Carbon quantum dots enriching molecular nickel polyoxometalate over CdS semiconductor for photocatalytic water splitting, *Appl. Catal. B: Environ.* 293 (2021), 120214, <https://doi.org/10.1016/j.apcatb.2021.120214>.
- [119] L. Qin, Y. Lin, Y. Dou, Y. Yang, K. Li, T. Li, F. Liu, Toward enhanced photocatalytic activity of graphite carbon nitride through rational design of noble metal-free dual cocatalysts, *Nanoscale* 12 (2020) 13829–13837, <https://doi.org/10.1039/C9NR10044J>.
- [120] D. Liu, J. Shen, Y. Xie, C. Qiu, Z. Zhang, J. Long, H. Lin, X. Wang, Metalliz Pt and PtO_2 dual-cocatalyst-loaded binary composite RGO-CN_x for the photocatalytic production of hydrogen and hydrogen peroxide, *ACS Sustain. Chem. Eng.* 9 (2021) 6380–6389, <https://doi.org/10.1021/acssuschemeng.1c00692>.
- [121] J. Cao, H. Wang, Y. Zhao, Y. Liu, Q. Wu, H. Huang, M. Shao, Y. Liu, Z. Kang, Phosphorus-doped porous carbon nitride for efficient sole production of hydrogen peroxide via photocatalytic water splitting with a two-channel pathway, *J. Mater. Chem. A* 8 (2020) 3701–3707, <https://doi.org/10.1039/C9TA13929J>.

- [122] Y. Wang, Y. Wang, J. Zhao, M. Chen, X. Huang, Y. Xu, Efficient production of H₂O₂ on Au/WO₃ under visible light and the influencing factors, *Appl. Catal. B: Environ.* 284 (2021), 119691, <https://doi.org/10.1016/j.apcatb.2020.119691>.
- [123] F. He, K. Li, C. Yin, Y. Wang, H. Tang, Z. Wu, Single Pd atoms supported by graphitic carbon nitride, a potential oxygen reduction reaction catalyst from theoretical perspective, *Carbon* 114 (2017) 619–627, <https://doi.org/10.1016/j.carbon.2016.12.061>.
- [124] A. Plauck, E.E. Stangland, J.A. Dumesic, M. Mavrikakis, Active sites and mechanisms for H₂O₂ decomposition over Pd catalysts, *Proc. Natl. Acad. Sci. U. S. A.* 113 (2016) E1973–E1982, <https://doi.org/10.1073/pnas.1602172113>.
- [125] M. Teranishi, S. Naya, H. Tada, In Situ liquid phase synthesis of hydrogen peroxide from molecular oxygen using gold nanoparticle-loaded titanium(IV) dioxide photocatalyst, *J. Am. Chem. Soc.* 132 (2010) 7850–7851, <https://doi.org/10.1021/ja102651g>.
- [126] D. Tsukamoto, A. Shiro, Y. Shiraishi, Y. Sugano, S. Ichikawa, S. Tanaka, T. Hirai, Photocatalytic H₂O₂ production from ethanol/O₂ system using TiO₂ loaded with Au–Ag bimetallic alloy nanoparticles, *ACS Catal.* 2 (2012) 599–603, <https://doi.org/10.1021/cs2006873>.
- [127] G. Moon, W. Kim, A.D. Bokare, N. Sung, W. Choi, Solar production of H₂O₂ on reduced graphene oxide–TiO₂ hybrid photocatalysts consisting of earth-abundant elements only, *Energy Environ. Sci.* 7 (2014) 4023–4028, <https://doi.org/10.1039/C4EE02757D>.
- [128] K. Fukui, R. Takioka, K. Iwamura, M. Todoroki, K. Sayama, N. Ikenaga, Photocatalytic H₂O₂ production from O₂ under visible light irradiation over phosphate ion-coated Pd nanoparticles-supported BiVO₄, *Appl. Catal. B: Environ.* 272 (2020), 119003, <https://doi.org/10.1016/j.apcatb.2020.119003>.
- [129] J.H. Lee, H. Cho, S.O. Park, J.M. Hwang, Y. Hong, P. Sharma, W.C. Jeon, Y. Cho, C. Yang, S.K. Kwak, H.R. Moon, J. Jang, High performance H₂O₂ production achieved by sulfur-doped carbon on CdS photocatalyst via inhibiting reverse H₂O₂ decomposition, *Appl. Catal. B: Environ.* 284 (2021), 119690, <https://doi.org/10.1016/j.apcatb.2020.119690>.
- [130] Y. Hong, Y. Cho, E.M. Go, P. Sharma, H. Cho, B. Lee, S.M. Lee, S.O. Park, M. Ko, S. K. Kwak, C. Yang, J. Jang, Unassisted photocatalytic H₂O₂ production under visible light by fluorinated polymer-TiO₂ heterojunction, *Chem. Eng. J.* 418 (2021), 129346, <https://doi.org/10.1016/j.cej.2021.129346>.
- [131] Y. Isaka, Y. Kawase, Y. Kuwahara, K. Mori, H. Yamashita, Two-Phase System Utilizing Hydrophobic Metal-Organic Frameworks (MOFs) for photocatalytic synthesis of hydrogen peroxide, *Angew. Chem. Int. Edit.* 58 (2019) 5402–5406, <https://doi.org/10.1002/anie.201901961>.
- [132] Y. Kawase, Y. Isaka, Y. Kuwahara, K. Mori, H. Yamashita, Ti cluster-alkylated hydrophobic MOFs for photocatalytic production of hydrogen peroxide in two-phase systems, *Chem. Commun.* 55 (2019) 6743–6746, <https://doi.org/10.1039/C9CC02380A>.
- [133] X. Chen, Y. Kuwahara, K. Mori, C. Louis, H. Yamashita, A hydrophobic titanium doped zirconium-based metal organic framework for photocatalytic hydrogen peroxide production in a two-phase system, *J. Mater. Chem. A* 8 (2020) 1904–1910, <https://doi.org/10.1039/C9TA1120D>.
- [134] X. Chen, Y. Kuwahara, K. Mori, C. Louis, H. Yamashita, Heterometallic and hydrophobic metal-organic frameworks as durable photocatalysts for boosting hydrogen peroxide production in a two-phase system, *ACS Appl. Energ. Mater.* 4 (2021) 4823–4830, <https://doi.org/10.1021/acsam.1c00371>.
- [135] Y. Liu, X. Zeng, X. Hu, Y. Xia, X. Zhang, Solar-Driven Photocatalytic Disinfection Over 2D Semiconductors: The Generation and Effects of Reactive Oxygen Species, *Solar RRL* 5 (2021) 2000594, <https://doi.org/10.1002/solr.202000594>.
- [136] Y. Liu, X. Zeng, X. Hu, J. Hu, Z. Wang, Y. Yin, C. Sun, X. Zhang, Two-dimensional g-C₃N₄/TiO₂ nanocomposites as vertical Z-scheme heterojunction for improved photocatalytic water disinfection, *Catal. Today* 335 (2019) 243–251, <https://doi.org/10.1016/j.cattod.2018.11.053>.
- [137] Z. Teng, N. Yang, H. Lv, S. Wang, M. Hu, C. Wang, D. Wang, G. Wang, Edge-Functionalized g-C₃N₄ nanosheets as a highly efficient metal-free photocatalyst for safe drinking water, *Chem* 5 (2019) 664–680, <https://doi.org/10.1016/j.chempr.2018.12.009>.
- [138] D. Xia, W. Wang, R. Yin, Z. Jiang, T. An, G. Li, H. Zhao, P.K. Wong, Enhanced photocatalytic inactivation of *Escherichia coli* by a novel Z-scheme g-C₃N₄ / m-Bi₂O₃ hybrid photocatalyst under visible light: The role of reactive oxygen species, *Appl. Catal. B: Environ.* 214 (2017) 23–33, <https://doi.org/10.1016/j.apcatb.2017.05.035>.
- [139] X. Hu, X. Zeng, Y. Liu, J. Lu, S. Yuan, Y. Yin, J. Hu, D.T. McCarthy, X. Zhang, Nano-layer based 1T-rich MoS₂/g-C₃N₄ co-catalyst system for enhanced photocatalytic and photoelectrochemical activity, *Appl. Catal. B: Environ.* 268 (2020), 118466, <https://doi.org/10.1016/j.apcatb.2019.118466>.
- [140] C. Liu, D. Kong, P. Hsu, H. Yuan, H. Lee, Y. Liu, H. Wang, S. Wang, K. Yan, D. Lin, P.A. Maraccini, K.M. Parker, A.B. Boehm, Y. Cui, Rapid water disinfection using vertically aligned MoS₂ nanofilms and visible light, *Nat. Nanotechnol.* 11 (2016) 1098–1104, <https://doi.org/10.1038/nnano.2016.138>.
- [141] Y. Chen, T.W. Ng, A. Lu, Y. Li, H.Y. Yip, T. An, G. Li, H. Zhao, M. Gao, P.K. Wong, Comparative study of visible-light-driven photocatalytic inactivation of two different wastewater bacteria by natural sphalerite, *Chem. Eng. J.* 234 (2013) 43–48, <https://doi.org/10.1016/j.cej.2013.08.106>.
- [142] X. Geng, L. Wang, L. Zhang, H. Wang, Y. Peng, Z. Bian, H₂O₂ production and in situ sterilization over a ZnO/g-C₃N₄ heterojunction photocatalyst, *Chem. Eng. J.* 420 (2021), 129722, <https://doi.org/10.1016/j.cej.2021.129722>.
- [143] S. Giannakis, M.I. Polo López, D. Spuhler, J.A. Sánchez Pérez, P. Fernández Ibáñez, C. Pulgarín, Solar disinfection is an augmentable, in situ -generated photo-Fenton reaction—Part 1: A review of the mechanisms and the fundamental aspects of the process, *Appl. Catal. B: Environ.* 199 (2016) 199–223, <https://doi.org/10.1016/j.apcatb.2016.06.009>.
- [144] J. He, Z. Zheng, I.M.C. Lo, Different responses of gram-negative and gram-positive bacteria to photocatalytic disinfection using solar-light-driven magnetic TiO₂-based material, and disinfection of real sewage, *Water Res.* 207 (2021), 117816, <https://doi.org/10.1016/j.watres.2021.117816>.
- [145] X. Xie, R. Wang, X. Zhang, Y. Ren, T. Du, Y. Ni, H. Yan, L. Zhang, J. Sun, W. Zhang, J. Wang, A photothermal and self-induced Fenton dual-modal antibacterial platform for synergistic enhanced bacterial elimination, *Appl. Catal. B: Environ.* 295 (2021), 120315, <https://doi.org/10.1016/j.apcatb.2021.120315>.
- [146] R. Zhang, C. Li, W. Liu, Y. Huang, B.O. Wang, K. Xiao, P.K. Wong, L. Ye, The photothermal synergy effect of pure Ti₃C₂T_x in antibacterial reaction and its mechanism, *Environ. Sci.: Nano* 8 (5) (2021) 1446–1455, <https://doi.org/10.1039/D0EN01293A>.
- [147] R. Zhang, C. Song, M. Kou, P. Yin, X. Jin, L. Wang, Y. Deng, B. Wang, D. Xia, P. K. Wong, L. Ye, Sterilization of *Escherichia coli* by photothermal synergy of WO₃-xNanosheet under Infrared Light Irradiation, *Environ. Sci. Technol.* 54 (2020) 3691–3701, <https://doi.org/10.1021/acs.est.9b07891>.
- [148] W. Fan, J. Cui, Q. Li, Y. Huo, D. Xiao, X. Yang, H. Yu, C. Wang, P. Jarvis, T. Lyu, M. Huo, Bactericidal efficiency and photochemical mechanisms of micro/nano bubble-enhanced visible light photocatalytic water disinfection, *Water Res.* 203 (2021), 117531, <https://doi.org/10.1016/j.watres.2021.117531>.
- [149] F. Feng, W. Yang, S. Gao, C. Sun, Q. Li, Postillumination activity in a single-phase photocatalyst of mo-doped TiO₂ nanotube array from its photocatalytic “memory”, *ACS Sustain. Chem. Eng.* 6 (2018) 6166–6174, <https://doi.org/10.1021/acssuschemeng.7b04845>.
- [150] J. Xiao, Q. Liu, M. Song, X. Li, Q. Li, J.K. Shang, Directing photocatalytic pathway to exceedingly high antibacterial activity in water by functionalizing holey ultrathin nanosheets of graphitic carbon nitride, *Water Res.* 198 (2021), 117125, <https://doi.org/10.1016/j.watres.2021.117125>.
- [151] X. Zeng, Y. Liu, Y. Xia, M.H. Uddin, D. Xia, D.T. McCarthy, A. Deletic, J. Yu, X. Zhang, Cooperatively modulating reactive oxygen species generation and bacteria-photocatalyst contact over graphitic carbon nitride by polyethylenimine for rapid water disinfection, *Appl. Catal. B: Environ.* 274 (2020), 119095, <https://doi.org/10.1016/j.apcatb.2020.119095>.
- [152] H. Song, L. Wei, C. Chen, C. Wen, F. Han, Photocatalytic production of H₂O₂ and its in situ utilization over atomic-scale Au modified MoS₂ nanosheets, *J. Catal.* 376 (2019) 198–208, <https://doi.org/10.1016/j.jcat.2019.06.015>.
- [153] H. Zhang, X. Bai, Photocatalytic production of hydrogen peroxide over Z-scheme Mn₃O₄/Co₉S₈ with p-n heterostructure, *Appl. Catal. B: Environ.* 298 (2021), 120516, <https://doi.org/10.1016/j.apcatb.2021.120516>.
- [154] A. Torres-Pinto, M.J. Sampaio, J. Teixo, C.G. Silva, J.L. Faria, A.M.T. Silva, Photo-Fenton degradation assisted by in situ generation of hydrogen peroxide using a carbon nitride photocatalyst, *J. Water Process. Eng.* 37 (2020), 101467, <https://doi.org/10.1016/j.jwpe.2020.101467>.
- [155] J. Ma, K. Wang, C. Wang, X. Chen, W. Zhu, G. Zhu, W. Yao, Y. Zhu, Photocatalysis-self-Fenton system with high-fluent degradation and high mineralization ability, *Appl. Catal. B: Environ.* 276 (2020), 119150, <https://doi.org/10.1016/j.apcatb.2020.119150>.
- [156] Z. Jiang, L. Wang, J. Lei, Y. Liu, J. Zhang, Photo-Fenton degradation of phenol by CdS/rGO/Fe²⁺ at natural pH with in situ-generated H₂O₂, *Appl. Catal. B: Environ.* 241 (2019) 367–374, <https://doi.org/10.1016/j.apcatb.2018.09.049>.
- [157] J. Zhang, G. Zhang, Q. Ji, H. Lan, J. Qu, H. Liu, Carbon nanodot-modified FeOCl for photo-assisted Fenton reaction featuring synergistic in-situ H₂O₂ production and activation, *Appl. Catal. B: Environ.* 266 (2020), 118665, <https://doi.org/10.1016/j.apcatb.2020.118665>.
- [158] Q. Liu, L. Zhou, L. Liu, J. Li, S. Wang, H. Znad, S. Liu, Magnetic ZnO@Fe₃O₄ composite for self-generated H₂O₂ toward photo-Fenton-like oxidation of nitrophenol, *Compos. Pt. B: Eng.* 200 (2020), 108345, <https://doi.org/10.1016/j.compositesb.2020.108345>.
- [159] Y. Wu, J. Chen, H. Che, X. Gao, Y. Ao, P. Wang, Boosting 2e oxygen reduction reaction in garland carbon nitride with carbon defects for high-efficient photocatalysis-self-Fenton degradation of 2,4-dichlorophenol, *Appl. Catal. B: Environ.* 307 (2022), 121185, <https://doi.org/10.1016/j.apcatb.2022.121185>.
- [160] S. Huang, Y. Xu, T. Zhou, M. Xie, Y. Ma, Q. Liu, L. Jing, H. Xu, H. Li, Constructing magnetic catalysts with in-situ solid-liquid interfacial photo-Fenton-like reaction over Ag₃Po₄@NiFe₂O₄ composites, *Appl. Catal. B: Environ.* 225 (2018) 40–50, <https://doi.org/10.1016/j.apcatb.2017.11.045>.
- [161] F. Xu, C. Lai, M. Zhang, B. Li, S. Liu, M. Chen, L. Li, Y. Xu, L. Qin, Y. Fu, X. Liu, H. Yi, X. Yang, Facile one-pot synthesis of carbon self-doped graphitic carbon nitride loaded with ultra-low ceric dioxide for high-efficiency environmental photocatalysis: Organic pollutants degradation and hexavalent chromium reduction, *J. Colloid Interf. Sci.* 601 (2021) 196–208, <https://doi.org/10.1016/j.jcis.2021.05.124>.
- [162] J. Xiong, X. Li, J. Huang, X. Gao, Z. Chen, J. Liu, H. Li, B. Kang, W. Yao, Y. Zhu, CN/GO@BPQDs high-low junctions with stretching spatial charge separation ability for photocatalytic degradation and H₂O₂ production, *Appl. Catal. B: Environ.* 266 (2020), 118602, <https://doi.org/10.1016/j.apcatb.2020.118602>.
- [163] Y. Wang, B. Jing, F. Wang, S. Wang, X. Liu, Z. Ao, C. Li, Mechanism Insight into enhanced photodegradation of pharmaceuticals and personal care products in natural water matrix over crystalline graphitic carbon nitrides, *Water Res.* 180 (2020), 115925, <https://doi.org/10.1016/j.watres.2020.115925>.
- [164] G. Moon, S. Kim, Y. Cho, J. Lim, D. Kim, W. Choi, Synergistic combination of bandgap-modified carbon nitride and WO₃ for visible light-induced oxidation of arsenite accelerated by in-situ Fenton reaction, *Appl. Catal. B: Environ.* 218 (2017) 819–824, <https://doi.org/10.1016/j.apcatb.2017.07.021>.

- [165] X. Li, J. He, J. Lu, Y. Zhou, Y. Zhou, In-situ production and activation of H₂O₂ for enhanced degradation of roxarsone by FeS₂ decorated resorcinol-formaldehyde resins, *J. Hazard. Mater.* 424 (2022), 127650, <https://doi.org/10.1016/j.jhazmat.2021.127650>.
- [166] G. Dong, L. Yang, F. Wang, L. Zang, C. Wang, Removal of Nitric Oxide through Visible Light Photocatalysis by g-C₃N₄ Modified with Perylene Imides, *ACS Catal.* 6 (2016) 6511–6519, <https://doi.org/10.1021/acscatal.6b01657>.
- [167] L. Yang, P. Wang, J. Yin, C. Wang, G. Dong, Y. Wang, W. Ho, Engineering of reduced graphene oxide on nanosheet-g-C₃N₄/perylene imide heterojunction for enhanced photocatalytic redox performance, *Appl. Catal. B: Environ.* 250 (2019) 42–51, <https://doi.org/10.1016/j.apcatb.2019.02.076>.
- [168] Y. Li, S. Ouyang, H. Xu, X. Wang, Y. Bi, Y. Zhang, J. Ye, Constructing solid-gas-interfacial fenton reaction over alkalinized-C₃N₄ photocatalyst to achieve apparent quantum yield of 49% at 420 nm, *J. Am. Chem. Soc.* 138 (2016) 13289–13297, <https://doi.org/10.1021/jacs.6b07272>.
- [169] Y. Zheng, Z. Yu, H. Ou, A.M. Asiri, Y. Chen, X. Wang, Black phosphorus and polymeric carbon nitride heterostructure for photoinduced molecular oxygen activation, *Adv. Funct. Mater.* 28 (2018) 1705407, <https://doi.org/10.1002/adfm.201705407>.